

# **Analysis on Plasma Sheath Formation and its Effects on Radio Communications**

a project presented to  
The Faculty of the Department of Aerospace Engineering San  
José State University

in partial fulfillment of the requirements for the degree  
*Master of Science in Aerospace Engineering*

by

**Jared Delatorre Wakefield Sagaga**

May 2018

approved by

Dr. Nikos Mourtos  
Faculty Advisor



# Table of Contents

<b>Chapter 1. Literature Review</b> .....	3
1.0 Project Objective .....	3
1.1 Introduction .....	3
1.2 Background.....	6
1.3 Methodology .....	10
<b>Chapter 2. Analysis</b> .....	12
2.0 Analytical .....	12
2.0.1 Euler Equations .....	13
2.0.2 Navier-Stokes Equations .....	14
2.1 Computational Fluid Dynamics (CFD) .....	15
2.1.1 Two-Dimension .....	16
2.1.2 Three-Dimension .....	16
2.1.3 Geometry/Fluid Domain .....	17
2.1.3 Grid Generation .....	21
2.1.4 Solver .....	23
<b>Chapter 3. Post-Analysis</b> .....	26
3.0 Results .....	26
3.1 Discussion.....	29
<b>Chapter 4. Radio Attenuation Measurement (RAM) Project</b> .....	30
4.0 Project RAM.....	30
<b>Chapter 5. Advanced Validation of CFD using a Navier-Stokes Solver</b> .....	36
5.0 Weakly Ionized Hypersonic Flows .....	36
5.1 Validation Analysis .....	45
<b>Chapter 6. Post-Analysis</b> .....	52
6.0 Results .....	52
6.1 Conclusion.....	60
6.2 Future Work .....	60
<b>7.0 Acknowledgements</b> .....	61
<b>8.0 References</b> .....	62
<b>9.0 Appendices</b> .....	67



# Chapter 1

## Literature Review

### 1.0 Project Objective

The study for this project will be focused on modeling and simulating the formation of plasma sheath including techniques are currently in the lead as a best possible solution. First, a geometric idealization of the body as a rigid structure, in this case, the Apollo Command Module (CM) has been selected. Then CFD simulations will be conducted in supersonic flow enveloping the entire environment in which the capsule exposed to. One of the critical conditions for the success of this project will be to have the correct chemical reactions in order to have results of high accuracy. Then the following list contains project milestones that are to be completed:

- Idealized CFD modeling, simulation, and analysis of the plasma flow field and the physics around a blunt body (Apollo CM)
- Complete knowledge of the aerodynamic and aerothermodynamic loading around the CM with emphasis on the heat shield during re-entry
- Complete knowledge of the techniques currently in research in order to resolve communications blackout and mitigate the plasma sheath from forming
- Analysis on the link budget for transmitting and receiving signals both with and without plasma sheath to better methods of getting signals through the plasma sheath
- Computational modeling and simulation flow of the Apollo CM during re-entry

### 1.1 Introduction

Studying or venturing everything within the occupying space of Earth and beyond has always been a part of the human race's curious mind for discovery. The human race has always been motivated to invent or innovate in order to survive, which is evident from the evolution of the technology we have created in order to sustain human life. That evolution of technology has

allowed for us to venture beyond Earth as well as to study the space which it occupies and beyond. Satellite communications as one of the many benefactors from the shift of technology whether it'd be analog to digital, or with almost every piece of hardware moving at the Nano level, has benefitted very much from this shift, allowing for increased performance and reduced risk-to-cost ratio. Data gathering from the vast space beyond is only possible due not only to satellites/satellite communications, but also the continued improved performance brought about telemetry solutions because of technology's evolution allowing for it to be possible. Some of the research involving space required people to not only travel beyond Earth's atmosphere, but to stationed out in space in to what we know as the International Space Station (ISS). The ISS is an engineering marvel, allowing for us to run experiments to learn more about how things behave in a gravity-less environment. However, with every new wave of innovation, that which helps improve technology, it is never absent with any problems.

One of the problems associated with satellite communications/telemetry is interference (e.g. noise), which concerns link budget, communications blackout (also known as plasma blackout), hardware deficiency, and/or technology availability. The magnitude of effects caused by interference is dependent on the type of system being looked at, whether it'd be cellular systems, TV broadcasts, weather systems, etc., it casts a very broad net affecting various systems and networks. An example for a disastrous possibility would be a military ballistics' tests (e.g. ICBM), where the guidance of the missile's trajectory is heavily dependent on real-time information provided by the GPS. Now, imagine if interference were to occur while the signals are being sent or received either by the GPS satellites or the projectile itself during flight, that could potentially put lives on the ground at risk. Because the real-time coordinates received by the missile's subsystems will either be delayed or incorrect due to the interference in the signals. Now one would think that from the command center, the missile can be aborted from there, however, due to the interference, that signal to abort or self-destruct might not reach the missile at all. For this one of many reasons, a great deal of research has gone into making sure that any flying vehicle manned or unmanned is to have no signal interferences hampering the success of a flight test or mission.

Another problem involving communications in general, has the same impact in terms of lives being in danger not only on the ground, but also those potentially in a re-entry vehicle. It is a problem that is crucial in ensuring not only the success of a re-entry mission, but also the lives of those in a re-entry vehicle, to do every possible that they are put in any kind of danger. A problem known as plasma blackout, which a phenomenon that has existed throughout the history of any space program. During a plasma blackout event, the communications between a space vehicle during re-entry and ground station are moot due to the signals from either side unable to reach one another. Plasma blackout is caused by the high temperatures that a re-entry

vehicle (manned or unmanned) experiences when the air in front of it heats up while decelerating while crossing the ionosphere. These high temperatures cause the gases within the ionosphere to ionize creating plasma (or a plasma sheath) which will be discussed more later on. The plasma sheath may envelop a space vehicle during re-entry as the shock ahead of it heats up the ambient gases and the ablation material of the heat shield. The effects of the plasma sheath can cause interruptions of radio communications between a space vehicle and ground station. The figure (Figure 2) below illustrates the plasma forming around a space vehicle during re-entry, the plasma conforms to the shape of that vehicle and depending on a vehicle's size, the plasma can also envelop it entirely. Problems that stem from this are a loss of voice communications and data telemetry during re-entry. In Figure 3, shows an experiment When this happens, it can last for a considerable amount of time, typically around ten to thirteen minutes, during the vehicle's most crucial part of its flight/descent back to earth.

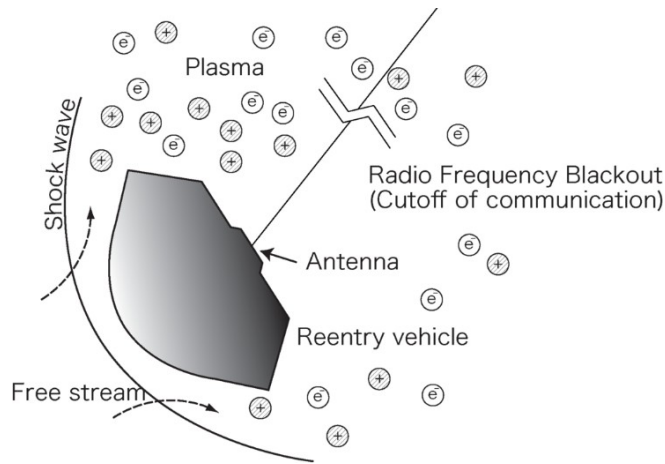


Figure 1. Plasma forming around space vehicle during re-entry (Takahashi, Nakasato, Oshima 2016)

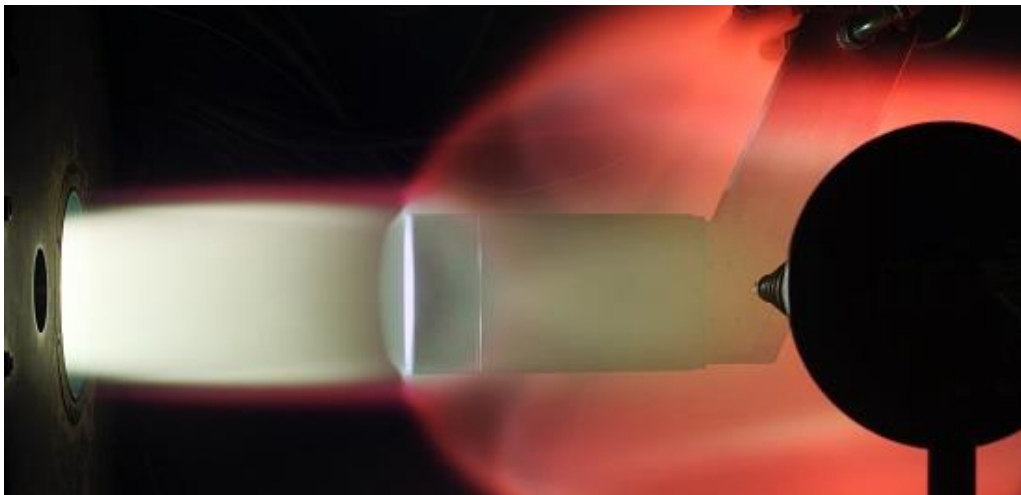


Figure 2. Test device placed inside hot gas flow (plasma) with antenna placed outside to receive signal (Messier 2016)

Studying this phenomenon and modeling it, a simulation of various situations of the plasma sheath's formation will prove useful in figuring out a solution for this problem which has plagued space programs around the world for numerous missions. The analytical and computational study will help in understanding any of the underlying physics of the plasma as well as the physics of the flow field of the region where the plasma sheath firsts forms. It will also help in understanding of the compressible flow in deceleration especially in first top regions of the earth's atmosphere. The outline for this study will include a complete historical background on any published works concerning this subject, a thorough review of any available literature and research that may provide crucial data gathered whether empirically or via simulations. The data gathered from the literature review will be serve as a benchmark for this study.

## 1.2 Background

Multiple past scientific investigations have developed the physics of the flow field and structure of a re-entry vehicle and its in-flight interactions while in the ionosphere, including other regions of the Earth's atmosphere (Figure 3). These investigations have been carried out both via software (e.g. CFD) and experimentally (e.g. tests performed in heated wind tunnels). The results from these investigations agree with one another confirming the parameters to which plasma formation takes place as well as enabling various solutions to be tried and tested in minimizing the formation of plasma.

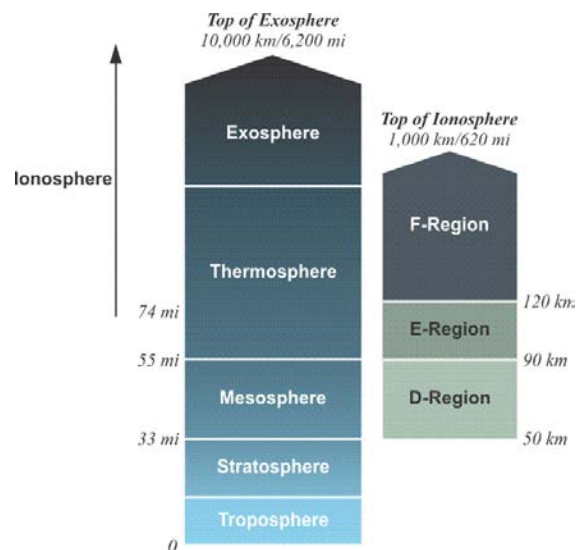


Figure 3. Model of Earth's atmospheric layers (Sickle 2017)

This signal interference between satellites and ground stations including others, stem mostly from when a radio signal passes through the ionosphere which is a region within the mesosphere, parts of the exosphere and thermosphere layers in the Earth's atmosphere. It is a

region split into three layers/zones labeled D, E, and F from the lowest to the highest in distance from Earth respectively. Due to the high energy from the Sun and the cosmos, the atoms of the gases in the Earth's ionosphere are ionized since they are stripped of one or more electrons therefore the ionized electrons behave as free particles. This ionized gas that exists in the ionosphere, is plasma, which is often referred to as the "fourth state of matter" alongside the principal states of matter – solid, liquid, and gas. Plasma not only forms around a space vehicle during re-entry, plasma can also already exist within the ionosphere. Now, how the plasma affects the radio signals (high frequency (HF) and shortwave signals) is by signal absorption or propagation which can be avoided and used as a benefit depending on the strength of the radio signal being sent or received. For example, radio waves below the plasma frequency, it's more likely that the signal will be reflected. However, radio waves with a frequency above the plasma frequency, the signal is more likely to be refracted, meaning it will bend while traveling through the regions of the ionosphere. As mentioned earlier, that ionized gas or plasma, can be a benefit, and that is to take advantage of the refraction caused by one of the regions in the ionosphere, allowing for signal propagation around the world. Since the ionosphere is not a uniform layer of plasma, its density changes throughout the day depending on multiple factors including the time of day, season, activity from the cosmos, and even solar activity. This variation in the plasma's density can cause problems in the propagation of signals since some of the radio signals are more likely to be absorbed rather than be reflected or bend. The higher the frequencies of the signal, lessens the chances for the signal to bend and at lower altitudes, radio signals tend to get absorbed (Sickle 2017) (Zubair, Haider, Khan, Nasir 2011) (Whitney, Basu 1977).

Ionospheric scintillation is another effect of the ionosphere on satellite communications, which is a rapid fluctuation in the strength of a signal from satellite to ground station and is caused by irregularities in the ionosphere. These irregularities are mostly patches or clumps of either high or low density of ionization and usually form in the auroral regions (north and south pole) as well as at the equatorial regions.

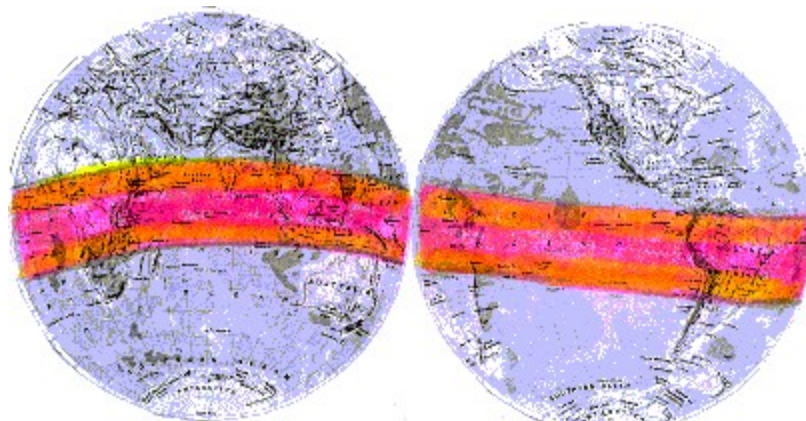


Figure 4. Scintillation effects (Kennewell, McDonald 2017)

The shaded areas in the figure above (Figure 4) show approximately the regions that are usually affected by the medium to strong scintillations. The affected regions with the most intense scintillation effects are towards the north and south edges of the shaded areas. Low frequency signals tend to experience worse effects of the scintillation as supposed to high frequency signals. Very high frequencies (VHF) suffer the most, L-band is moderately affected, and C-band or anything above are affected by the strongest scintillations. One of the ways that can be used to combat this problem is that since ionospheric scintillation occurs at certain times during the day, there's a possibility of scheduling most of the traffic, to have peak demand not to occur during evening hours. If not, then the alternative would be to use a different link at the time the effect is highest (Kennewell, McDonald 2017) (Hussein 2009).

Due to these various effects on radio frequency (RF) signals, it is a critical matter that during re-entry especially for a manned spacecraft, the communications between it and ground station are interference-free. This is because as the spacecraft re-enters the Earth's atmosphere, precise guidance from ground station and maneuvering by the crew are essential in the success of the return mission especially during the first phase of re-entry, decelerating to suborbital velocity. If ever manual maneuvering were required in the case of an emergency, it becomes much crucial for a communications link between ground station and spacecraft to be uninterrupted. As the spacecraft continues its re-entry and the formation of the ionized flow (plasma) forms around the spacecraft and its antenna making it extremely difficult for any type of communication to work. The interaction between the ionized flow and the spacecraft's radio antenna degrades its overall performance. Other arising problems include tracking errors, which rises from the Doppler range rate measurements as well as skin tracking becomes unreliable due to the confusion that the ionized vehicle's trail introduces, along with the precursor ionization in front of the shock ahead of the spacecraft. And so, in order to be better suited for this phenomenon, effects of plasma on communications have to be better understood and the degradation effects to be evaluated with high accuracy. Two problems arise when trying to analytically investigate this phenomenon, that is one, figuring out its properties, and two, the antenna's behavior when enveloped or near the plasma sheath. However, studying this phenomenon has been proven difficult for many scientists and space agencies around the world not only due to a lack of physical data, but also due to intransigent mathematical problems making it highly difficult to model. Constants for reaction rates for various chemical reactions are only crudely known. There are also constants for recombination rates by numerous authors have theoretically predicted, however, each one differs from each other in orders of magnitude of as much as three. To further highlight the difficulty set by this phenomenon, is its interaction with the antenna when immersed into the plasma sheath where the observed signals have been attenuated 20 dB or more, the difference in signal propagation are so harsh that the antenna radiation pattern will be completely different when the plasma is absent (Lehnert, Rosenbaum

1965). Even with the difficulty posed by this non-equilibrium phenomenon, the advances of plasma sheath/blackout research, CFD, and many other tools available today, that the roadblock into solving these problems have greatly minimized.

A number of techniques have been proposed in order to minimize or prevent communications blackout. Operating at a frequency much higher compared to the plasma's peak frequency expected during re-entry. This technique is not only expensive in terms of the link budget, because the frequency would have to be in excess of 10 GHz, the cost for securing and installing the equipment at more than one location is another roadblock. Laser signals is another interesting proposal, however, they get highly attenuated by the plasma. Another technique is shaping the re-entry vehicle aerodynamically as thin as possible which has proven to work, but it reduces the payload capability and increases heating as supposed to one with a blunt body. Generating magnetic fields around the antenna would create a magnetic window to which electromagnetic (EM) waves can propagate. This technique however, will increase weight making it impractical. Adding electrophilic materials into the plasma sheath upstream from the antenna location reducing the effects of the plasma sheath. How it works is that the electrophilic material flows out and readily combines with free electrons (which is the what is mostly in the ionized flow) and lowers the plasma frequency substantially. Early research of the technique was conducted by Rosen (1962) stating that injecting micron size refractory dust particles into the plasma sheath would reduce the plasma frequency due to it lowering the free electron density. There have been actual flight tests for testing out this technique which have been successful which was the RAM C-C flight. There has a been recent proposal for a viable solution to resolving the blackout communications issue, however, would still require more research and a validation via a flight tests or plasma wind tunnel tests. Forming a layer of an electrostatic sheath using two-dimensional shaped electrodes. Once the electrostatic sheath's size is comparable to the size of the transmission antenna, then transmitting signals through the plasma sheath may be possible during the time of the plasma blackout. This technique is based on depleting the electron density for the electrostatic sheath to form in its place (Rybak 1970) (Gillman, Foster, Blankson 2009) (Kim 2009).

Computational modeling and simulation efforts in the last couple of years have been very influential in the techniques that are in the lead for mitigating communications blackout. However, having the exact knowledge on the flow field's chemical environment is very crucial for predicting the formation of the plasma sheath especially minimizing its effects. A strong example of knowing these parameters in order to prevent communications blackout, is the Columbia incident in 2003, where all 7 members of Columbia crew lost their lives in a fatal explosion during re-entry flight. Telemetry from that return mission was lost prior to the explosion and this was due to a communications blackout. Only a handful of data from ground station was recovered,

but wasn't enough to assist in finding out what went wrong (Muylaert, Walpot, Ottens, Cipollini 2007). Computational studies have helped a great deal, it provides a better alternative in terms of expenses spent for flight tests (manned/unmanned). There have also been tests in plasma wind tunnels have been conducted not only by numerous research institutions, but also including academia. There has been a huge effort in converging for a solution to resolve plasma blackout, especially with more missions being planned for Mars including sending people there in the foreseeable future. Having complete knowledge of the harsh environment of plasma during re-entry will dictate the success and safety of future missions.

## **1.3 Methodology**

Focus of this project study is to understand the formation of plasma sheath and its effects on the radio communications including techniques currently being researched to mitigate those effects. For this study to be successful and meet its objective(s), analytical studies need to be conducted by utilizing the equations of motion fundamentally (e.g. Navier-Stokes Equations). In order to do so will require a computational study conducted via CFD (Computational Fluid Dynamics). This approach has been selected due to the nature of the subject as well as many other factors that need to be considered. Conducting a full scale 1:1 experiment of the Apollo in a plasma wind tunnel will be very expensive and resource intensive. CFD provides for a more accessible and provides more range in terms of the parameters/variables are to be included in this study.

A good engineering problem-solving technique to model and solve this subject is much more feasible and less of an expensive burden especially with a successful development of a computational study (e.g. CFD). To carry out a successful CFD, steps need to be taken to realize it which starts with a CAD model. The CAD model will be very watered-down version of the Apollo CM, the geometry and size will be the most important key aspect to look at and will be created using SolidWorks. The next step will be to generate a mesh for the CAD model. A structured mesh will be created using a commercial software, ESI, after the CAD model is imported into the software. An alternative for the mesh is a software called GridPro, which will be considered if results are unsatisfactory. Before concluding this step, a substantial amount of time must be spent on understanding the flow field topology including the object of interest. The topology of the mesh will be identified as near the object's surface, nearby outer boundaries, and the intermediate regions interfacing the two. Refining of the mesh will have it be finer near the surface of the object and coarser moving away and towards the far field. This is crucial due to computational time and resources are to be spent where the focus/location of the simulation is most needed, near the object.

The boundary conditions for the mesh will be as followed:

- Wall at object's surface
- Freestream inlet near the object (left)
- No slip condition
- Outflow near the object (right)

Model for the flow will be most likely be turbulent, however, laminar (inviscid) will be simulated to see the flow's behavior initially. After completing a few initial rounds of simulations, the results will be compiled and compared against any experimental/simulation data (if available) including those from published work. The development of this project's will dictate whether additional investigations will be made including a look at the link budget analysis. However, the main goal of this study is to understand the physics of the formation of the plasma and its effects on communications as well as reviewing techniques that could be possible and viable solutions.

# Chapter 2

## Analysis

### 2.0 Analytical

With today's applications in the aerospace industry getting more complicated not only with the physics involved, but also the design study to accommodate the complex physics that occur within that application. Before the rise of computing power that exists now, only analytical methods existed where extensive hand calculations were possible to resolve whatever the problem. However, presently that is not the case anymore with computer resources keep piling on along with the raw power that a single computer processor possesses today, that has helped those who conduct CFD in a tremendous effort in lowering the turnaround time for a solution. Not only has it sped up getting results back, it has allowed for more high-fidelity results not only between various CFD solvers, but also between simulation and experimental. The cost of performing an analysis has dramatically gone down creating huge savings in both money and time for various industries. While analytically is still looked at for much smaller cases, it cannot be argued that CFD isn't considered as the first approach due to the many advantages that it has. However, that is regarding whether the case being looked at is appropriate for a CFD analysis.

There are many other types of analysis methods to which computers can now perform and provide quick turnarounds such as Finite Element Analysis (FEA), Ice accretion simulations, Traffic flow simulations, and many more. With regards to CFD, advances are being made at a rapid pace enabling researchers, engineers, and scientists to conduct their experiments on many scales due to the advances on not only in the software, but also from in computing power. As advances are made to benefit not those who conduct CFD analysis, the cost also increases due to the complexity of the cases being looked at. Take for example the geometry of a space launch vehicle, there are much more instruments (e.g. sensors) on-board than there was twenty years, and this creates either cavities or protrusions on it since the instrument might require exposure to the atmosphere. The more complex the geometry, the more the difficult the physics model, which also in turn increase the required computing resources to resolve the simulation. For the purposes of this project, the analytical methods will not be looked at in terms of hand calculations, however, it is important to discuss it in some detail since it is used by CFD solver used for this project. The equations that will be discussed in the next few sections are the Euler equations and Navier-Stokes equations. However, majority of the simulations conducted in the analysis are using Euler's equations due to small effects of the viscosity in terms of the problem

for this project, which is re-entry. The two are very much the same nonetheless with the Euler having the absence of any viscosity effects, the Navier-Stokes equations are reduced down to the it due to that absence or its very small effect on the problem.

## 2.0.1 Euler Equations

One of two of the governing equations of the case being looked at in this master's project. As mentioned earlier, if the viscosity effects are neglected due to its effect being on a small scale, the Navier-Stokes equations are reduced to the Euler equations. In two-dimensional (Cartesian coordinates), the Euler equations can be represented as

$$\frac{\partial Q}{\partial t} + \frac{\partial E}{\partial x} + \frac{\partial F}{\partial y} = 0 \quad (1)$$

where

$$Q = \begin{bmatrix} q_1 \\ q_2 \\ q_3 \\ q_4 \end{bmatrix} = \begin{bmatrix} \rho \\ \rho u \\ \rho v \\ e \end{bmatrix}, E = \begin{bmatrix} \rho u \\ \rho u^2 + p \\ \rho uv \\ u(e + p) \end{bmatrix}, F = \begin{bmatrix} \rho v \\ \rho uv \\ \rho v^2 + p \\ v(e + p) \end{bmatrix}$$

where pressure,  $p$ , is related to the quantities which are conserved in the equation of state

$$p = (\gamma - 1) \left( E - \frac{1}{2} \rho (u^2 + v^2) \right)$$

in which  $u$  and  $v$  are the velocity components in Cartesian,  $\rho$  is the fluid density,  $e$  is the total energy per unit volume, and  $\gamma$  is the specific heat capacity. There are more than several methods that exist today to solve these equations for a given fluid flow problem which will be discussed later. Studying compressible flows at high Mach numbers, using Euler equations has often been the approach. Because viscous effects are neglected, the fluid is often assumed to be inviscid allowing for it not to stick to walls and making the slip condition possible for the boundary conditions at the wall. Viscous effects are still an important parameter to study, however, at high velocities, those effects are only important in small regions near the walls.

## 2.0.2 Navier-Stokes Equations

In the previous section, the Euler equations were briefly discussed being the reduced form of the Navier-Stokes equations due to the viscous effects being neglected. The Navier-Stokes equations consists of three different components which are, continuity, momentum, and energy. These components are time-dependent, therefore, one time-dependent continuity equation for conservative of mass, three time-dependent conservation of momentum equations and one time-dependent conservation of energy equation. Normally, the Navier-Stokes equations are three-dimensional, however, for this project, two-dimensional will suffice. The three-dimensional representation of the Navier-Stokes equations are as follows

- Continuity:

$$\frac{\partial \rho}{\partial t} + \frac{\partial(\rho u)}{\partial x} + \frac{\partial(\rho v)}{\partial y} + \frac{\partial(\rho w)}{\partial z} = 0 \quad (2)$$

- X-Momentum:

$$\frac{\partial(\rho u)}{\partial t} + \frac{\partial(\rho u^2)}{\partial x} + \frac{\partial(\rho uv)}{\partial y} + \frac{\partial(\rho uw)}{\partial z} = -\frac{\partial P}{\partial x} + \frac{1}{Re_r} \left( \frac{\partial \tau_{xx}}{\partial x} + \frac{\partial \tau_{xy}}{\partial y} + \frac{\partial \tau_{xz}}{\partial z} \right) \quad (3)$$

- Y-Momentum:

$$\frac{\partial(\rho v)}{\partial t} + \frac{\partial(\rho v^2)}{\partial y} + \frac{\partial(\rho uv)}{\partial x} + \frac{\partial(\rho vw)}{\partial z} = -\frac{\partial P}{\partial y} + \frac{1}{Re_r} \left( \frac{\partial \tau_{xy}}{\partial x} + \frac{\partial \tau_{yy}}{\partial y} + \frac{\partial \tau_{yz}}{\partial z} \right) \quad (4)$$

- Z-Momentum:

$$\frac{\partial(\rho w)}{\partial t} + \frac{\partial(\rho w^2)}{\partial z} + \frac{\partial(\rho uw)}{\partial x} + \frac{\partial(\rho vw)}{\partial y} = -\frac{\partial P}{\partial z} + \frac{1}{Re_r} \left( \frac{\partial \tau_{xz}}{\partial x} + \frac{\partial \tau_{yz}}{\partial y} + \frac{\partial \tau_{zz}}{\partial z} \right) \quad (5)$$

- Energy:

$$\begin{aligned} \frac{\partial(E_T)}{\partial t} + \frac{\partial(uE_T)}{\partial x} + \frac{\partial(vE_T)}{\partial y} + \frac{\partial(wE_T)}{\partial z} &= -\frac{\partial(uP)}{\partial x} - \frac{\partial(vP)}{\partial y} - \frac{\partial(wP)}{\partial z} \\ &= \frac{1}{Re_r Pr_r} \left( \frac{\partial q_x}{\partial x} + \frac{\partial q_y}{\partial y} + \frac{\partial q_z}{\partial z} \right) + \frac{1}{Re_r} \end{aligned} \quad (6)$$

$$\left( \frac{\partial}{\partial x} (u\tau_{xx} + v\tau_{xy} + w\tau_{xz}) + \frac{\partial}{\partial y} (u\tau_{xy} + v\tau_{yy} + w\tau_{yz}) + \frac{\partial}{\partial z} (u\tau_{xz} + v\tau_{yz} + w\tau_{zz}) \right)$$

where there are three dependent variables,  $x$ ,  $y$ , and  $z$  of a spatial domain as well as time  $t$ . Then rest of the variables are independent include  $p$  for pressure,  $\rho$  for the density, and  $T$  for the temperature. The three components for velocity are  $u$ ,  $v$ , and  $w$ . As mentioned earlier, this project will be dealing with two-dimensional cases, therefore, terms with the  $z$  spatial coordinate will drop out.

## 2.1 Computational Fluid Dynamics (CFD)

Fluids, whether it'd be gas or liquid, are governed by partial differential equations (PDEs) and these equations represent the various laws of conservation, mass, momentum, and energy. Before computers, doing everything by hand was the norm, resolving to analytical methods which could take hours, days, months, and even years to come to a general solution of results. Now, computers can be made as small as smartphones which are much more powerful than any other laptop that existed twenty years. With CFD, the turnaround on the results have been expediently fast, making it the first approach for most fluid flow problems. The qualitative or even quantitative predictions provided by CFD done so by modeling PDEs, utilizing numerical methods that involve different discretization or solution techniques, and using a variety of software tools with in-house solvers as well as pre/post processing tools. This has allowed engineers, researchers, and scientists to run experiments, mainly numerical, in a virtual laboratory. Many of the applications today in various industries have relied on the results generated from these simulations. CFD does not in any way replace experiments, it is, however, a way of validating the experimental data to ensure that any anomalies or phenomenon (if any) are captured either in the experiments or simulations. CFD simulations can never be one-hundred percent reliable regardless of whether it involved high-fidelity results. Various issues can cause for the simulations' accuracy to be reduced such as:

- Too much erroneous guessing or imprecision on the input data
  - Computing resources/power limiting the results' accuracy
  - Inadequate mathematical models used in the simulation

However, that does not mean that CFD is unreliable. It is still the top approach for a plethora of applications, providing high-fidelity results against experiments. A huge advantage that CFD has

as supposed to doing an experiment, is that, it's inexpensive, faster, portable, flexibility, easy-to-use, and multipurpose. For experiments, it's very much the opposite, which is more expensive, slower in getting results, single purpose, and a lot more difficult if something needed to change or if equipment needed to be moved. Other advantages that CFD have is the ability to work with complex cases inexpensively. Take the geometry for example, it might have features that could prove difficult to manufacture and get within a reasonable time frame which prolongs the process and the time to get back results for analysis. With CFD, it is extremely feasible with the technology that exists today or even twenty or thirty years when it was still a novelty for many people. CFD provides an insight into flow patterns that could be expensive, difficult or even impossible for traditional experimental techniques.

### **2.1.1 Two-Dimensional | Three-Dimensional**

Before the project was still an idea, that also included the process of deciding whether this problem should be looked in two or three dimensions. However, it can be thought going the three-dimension route should be the obvious choice, that would be a mistake. Either one is a suitable approach for this project's problem, but only one would be a better approach regarding the geometry. The Apollo (AS-202) command module is the main object of interest for this CFD analysis and because of its shape, a two-dimensional model of it will suffice. Reason being, is that the Apollo command module's shape is axisymmetric, which made things simpler. It is more than possible to create a three-dimension model of the command module and conduct a CFD analysis on it, however, due to it being axisymmetric, it would be a waste of computing power. The solution for axisymmetric (2D) and three-dimensional are typically very similar to each other. With a two-dimensional model of the command module, the problem is simplified so is the number of equations to be solved by the CFD solver. Before showing some images that showcase the process, there is a flowchart for the methodology:

### **Methodology in CFD**

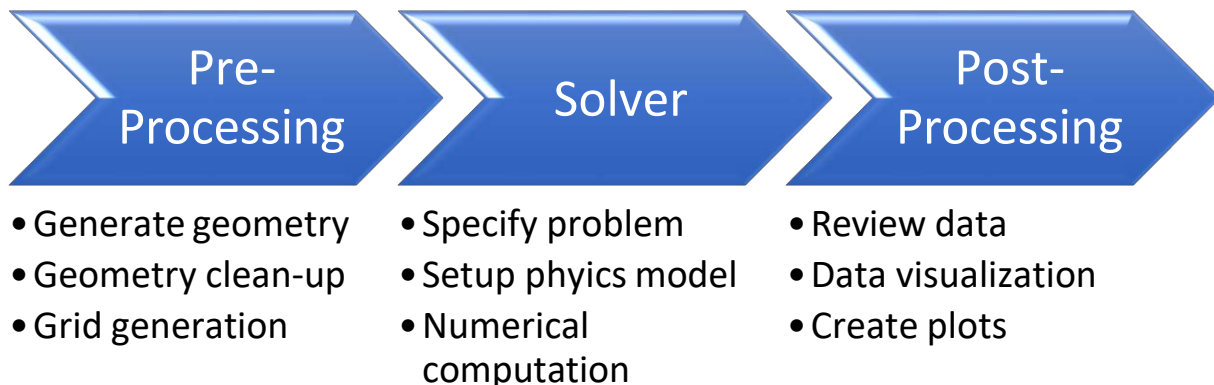


Figure 5. CFD Process

The methodology above gives an overview of the process for this project, which is also very similar to the process done in many other CFD analyses. The geometry clean-up, grid generation, and physics setup, are the most critical areas to get right because if any of those steps, the results will surely suffer in accuracy. Regardless of whether the simulation has converged to a solution, if the geometry was incorrect in some area or if the mesh was too coarse, the results are not as reliable. Any good practitioner of CFD will know that something is awry either from visualizations of the results or examining the residuals for odd behaviors in the convergence.

## **2.1.2 Geometry | Fluid Domain**

In the figures displayed below, shows the geometry of both the Apollo command module and the fluid domain which represents both the environment being simulated along with the command module. Several iterations were made in the design of the geometry, mostly on the fluid domain. The last design iteration was the one selected after several attempts of narrowing it down to what is most to see from the simulation results including other factors.

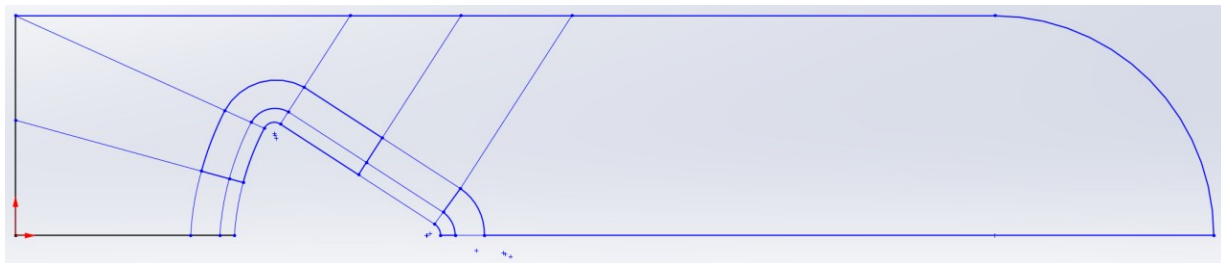


Figure 6. Design iteration 1.0

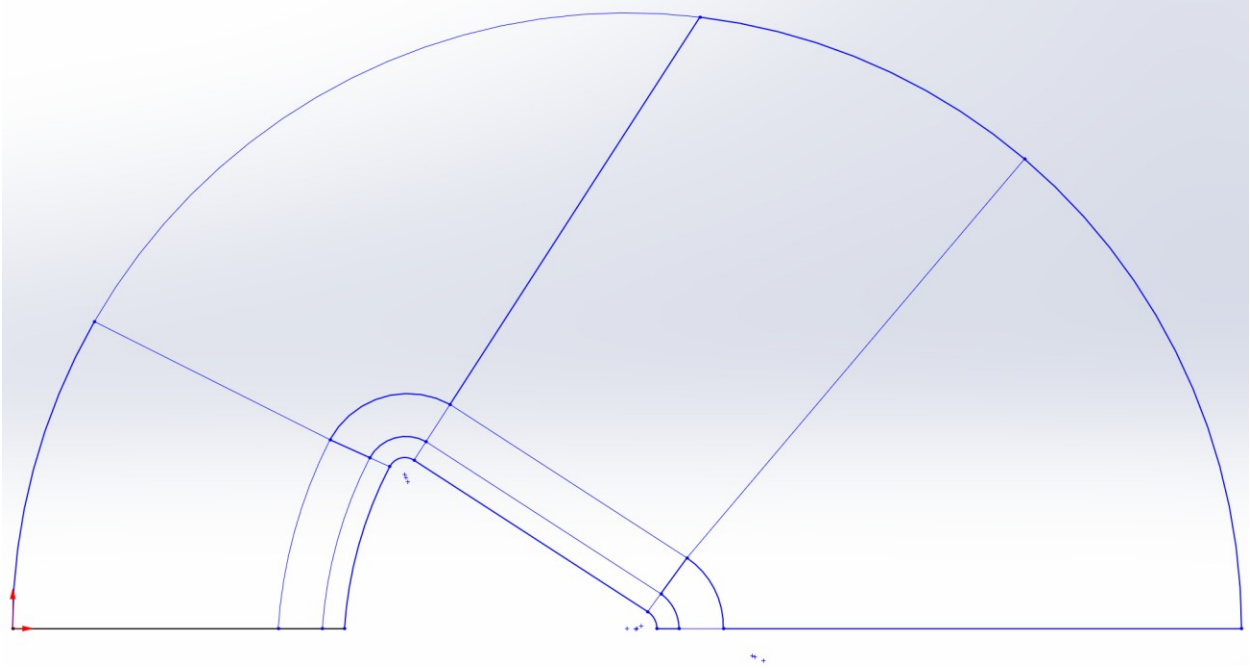


Figure 7. Design iteration 2.0

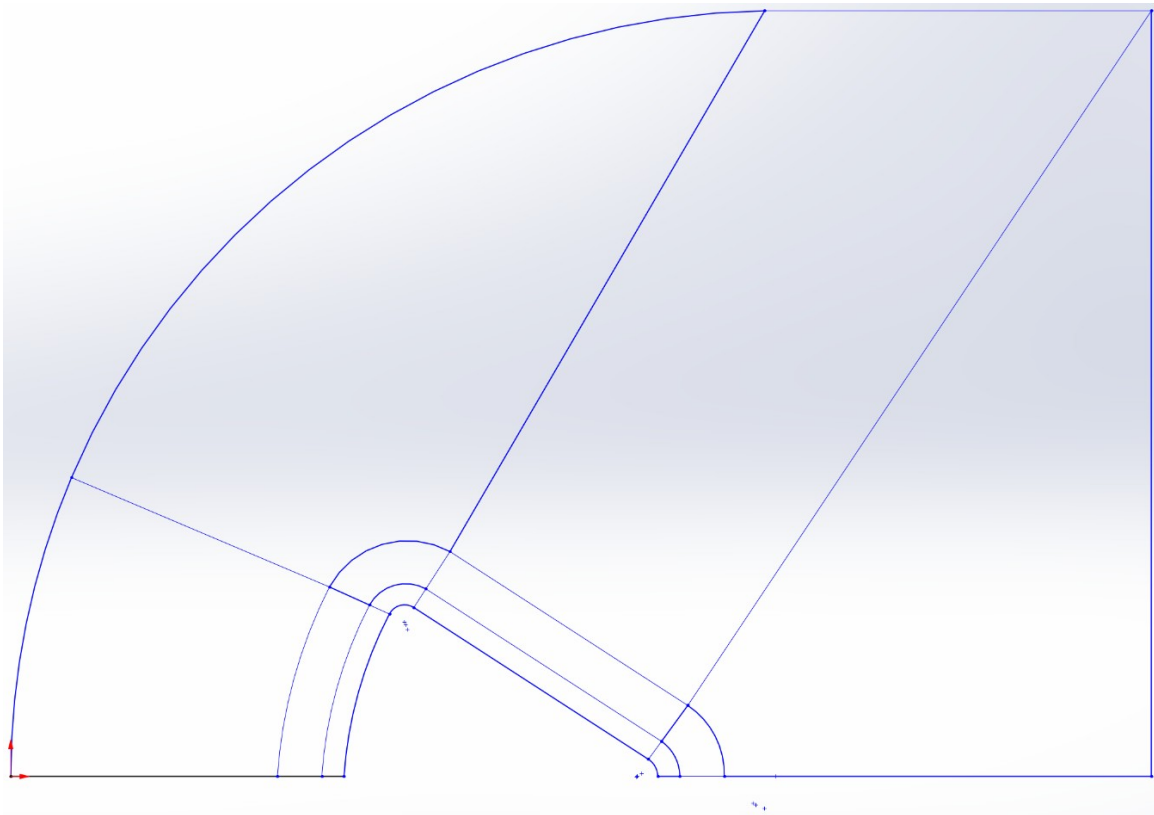


Figure 8. Design iteration 3.0

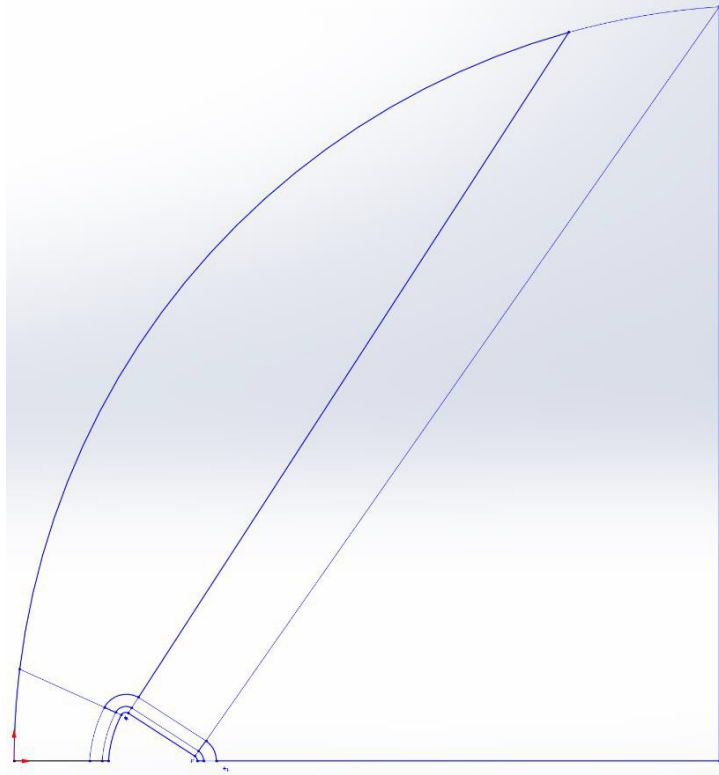


Figure 9. Design iteration 4.0

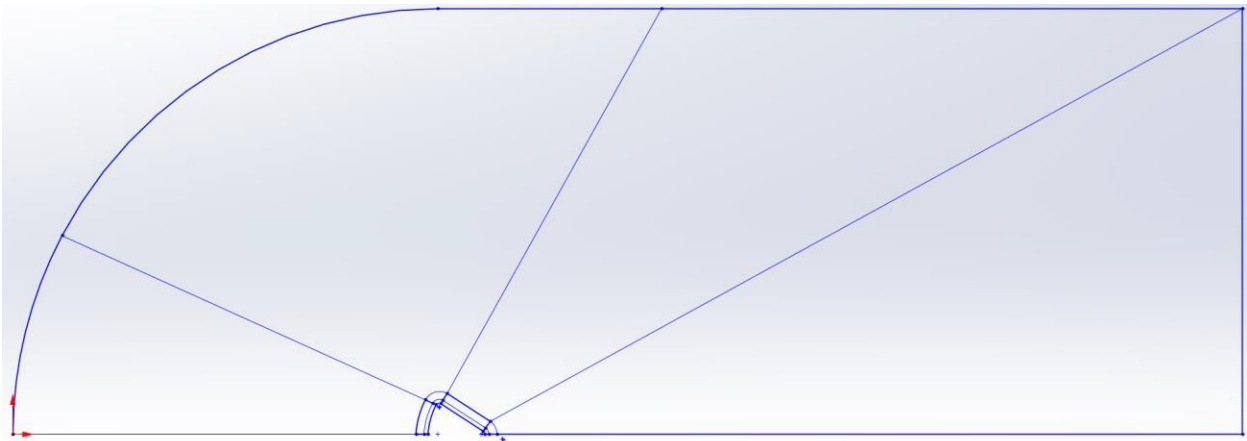


Figure 10. Design iteration 5.0

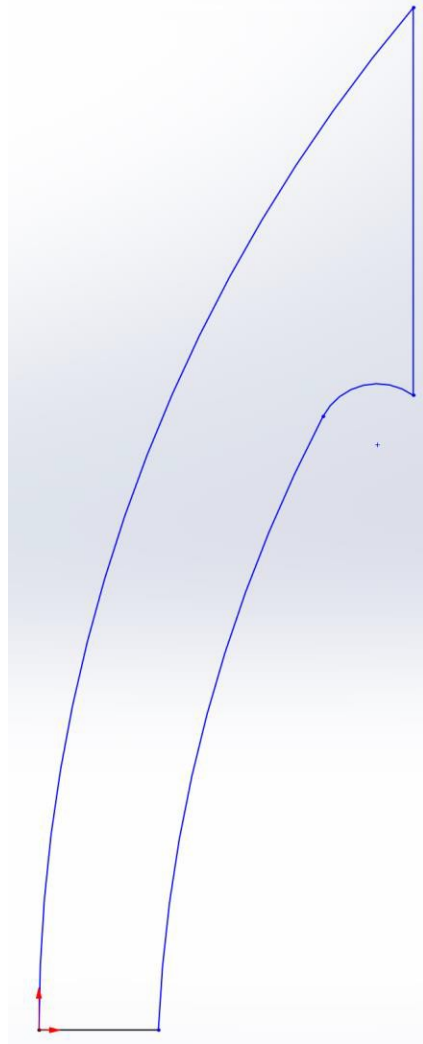


Figure 11. Design iteration 6.0

Examining the design iterations prior to 6.0, there several problems that would either make the mesh generation process to difficult, waste computing resources on unnecessary regions of the fluid domain, or the fluid domain was too big which changed the overall environment of the situation that is being simulated. Design iterations 3.0, 4.0, and 5.0 (Figures 7, 8, 9 respectively), the fluid domain was overstretched to where the boundary conditions were in the farfield away from the wall. Not only was the fluid domain overstretched onto unnecessary regions, that led to increased time for the solver. The boundary conditions needed to be closer to the wall to shrink down the overall fluid domain. Design iterations 1.0 and 2.0 were a mix of both overstretched the fluid domain, but also difficult for generating the mesh including creating the boundary conditions which had a few conflicts with one another. Considering all of mistakes made in design iterations 1.0 to 5.0, those issues were resolved and used to create the final design, design iteration 6.0, which is drastically different from the ones prior to it. Design iteration 6.0 removed most of what's in the previous iterations, but it also reduced the total cell count,

simplified the topology, and it was more ideal in terms of capturing what was going to be analyzed after running the simulations. The selected design would be more feasible if this was to be recreated for a different solver, so the pre-processing time would be reduced from the simplification.

### **2.1.3 Grid Generation**

Grid generation is a process where the fluid domain, which represents the environment in which the object of interest is placed in, gets divided up into pieces called cells and this allows for a solver to compute the overall fluid flow and its interactions with the object of interest. Generating the mesh, can take time depending on the scale and complexity of the geometry. For this project, the figures in the previous show how much the fluid domain from the first iteration to the final iteration which was selected. As mentioned earlier, the final design iteration, 6.0, had a much smaller fluid domain including its overall scale being much smaller compared to the prior iterations. The smaller scale and fluid domain allowed for the boundary conditions to be in the near field and closer to the wall. Since the focus of this project is to recreate the plasma which occurs during re-entry, all the other aerodynamic occurrences were unnecessary (e.g. shocks, wake, etc.). Not only did this allow for the analysis to be focused on the formation plasma sheath, it also cut down the total cell count and simplifying the fluid domain, decreasing the overall computational workload. This makes it possible to perform the simulations on a laptop, since it's two-dimensional, the fluid and geometry have been simplified, and the total cell count greatly reduced greatly reducing the need for computing resources.

The grid generation software used for generating the mesh was CFD-GEOM, a part of the ESI-CFD software package. CFD-GEOM is quite versatile, being able to create and manipulate imported geometry, and generating various types of mesh very quickly whether it's a multi-block structured/unstructured, polyhedral, overset, or hybrid. In the figure below, shows the completed mesh generation for design iteration 6.0, a structured mesh, using a power law distribution value of 2.0 for both the symmetry plane and outlet to increase the cell density near the wall. The power law distribution (Eqn. 7) is a method in which a change in one term or quantity, causes a proportional relative change onto another.

- Power law distribution:

$$u[n] = \left( \frac{n-1}{npts-1} \right)^x \quad (7)$$

where

$u[n] = n^{th}$  grid point on the interval

$[0 \dots 1]$ ,  $n =$  grid points index on the interval

$[1 \dots npts]$ ,  $npts =$  number of grid points

$x =$  user-defined power

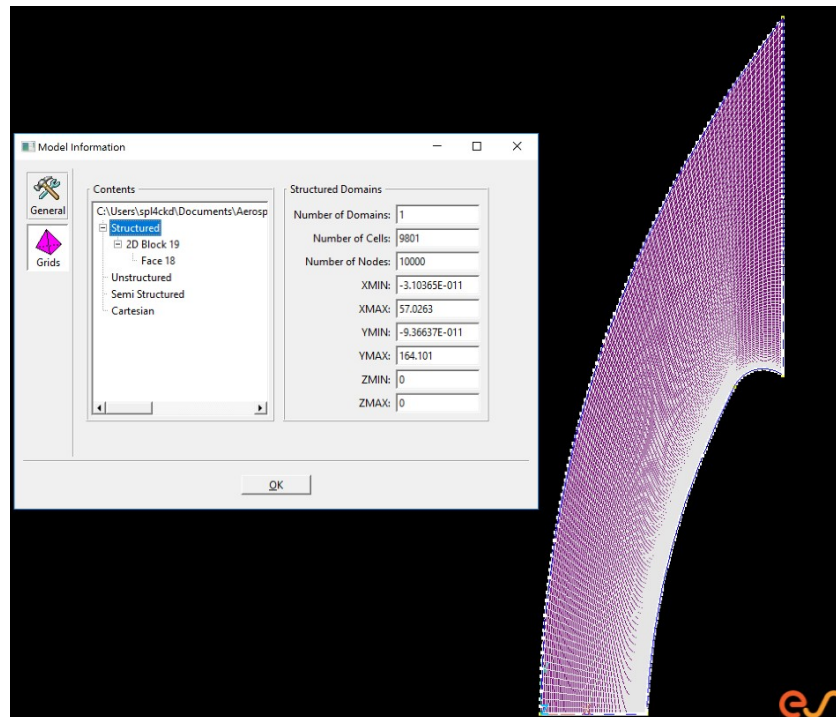


Figure 12. Design iteration 6.0 mesh

The total cell count for the mesh generation of design iteration 6.0 was 9,801 with 10,000 nodes and this is a significant reduction from the mesh generation of prior design iterations which range anywhere from 48,000 cells to 780,000 cells. However, the prior design iterations have one distinct difference compared to design iteration 6.0 and that is the geometry of the command module. Instead of simulating the entire the command module, only the heat shield was included into the final overall geometry of the fluid domain and command module. By doing this, the objective of this project doesn't need to be isolated which was the case in prior design iterations with a significantly larger fluid domain. With design iteration 6.0, the entire fluid domain which has been significantly reduced, removes unnecessary disturbances that would've been captured in the simulation had that not been the case. Importing the mesh into the solver is the next step in the pre-process of the CFD methodology.

## 2.1.4 Solver

In this part of the CFD analysis process, the mesh generated in the previous section is imported into CFD-FASTAN, which is one of the two simulation software that are included in the ESI-CFD software package. CFD-FASTAN has both Euler and Navier-Stokes solvers, enabling multiple types of applications to be simulated. Another feature of this software which enables for this project's cases to be simulated is having a generalized finite chemistry module. This module allows for the possibility of chemical reactions which is a critical requirement since it's an integral part of the plasma sheath formation. In the figure below (Figure 13) is a snippet of CFD-FASTAN along with the databases where the five chemical reactions are listed below and the physics setup.

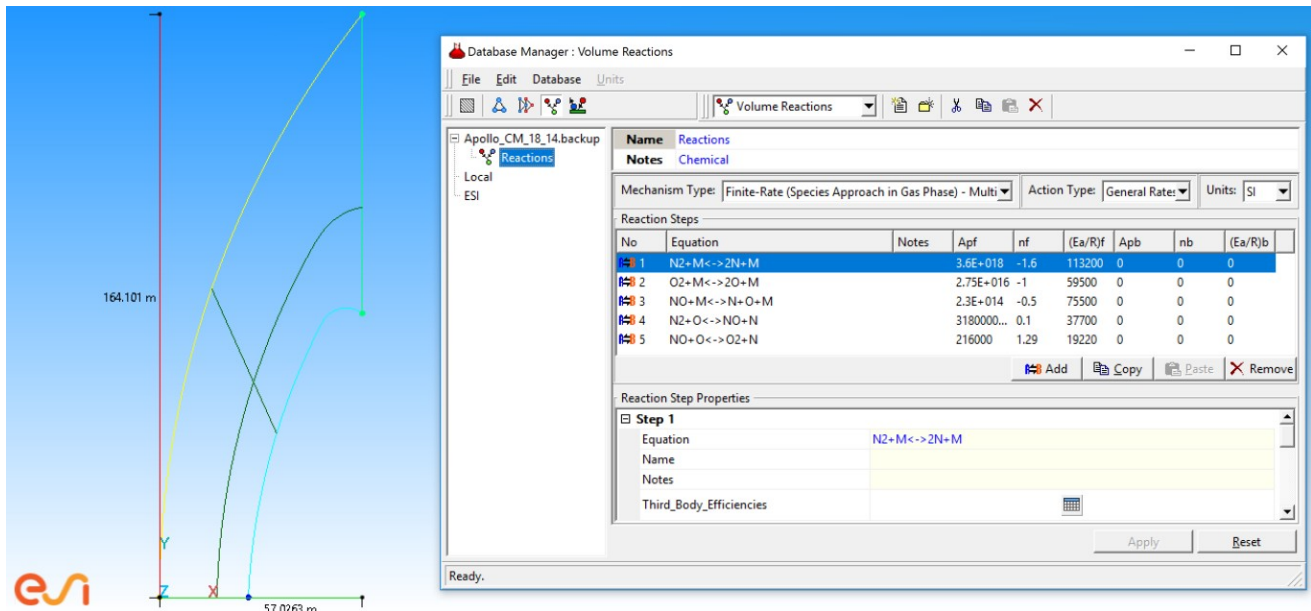


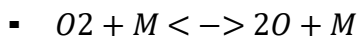
Figure 13. CFD-FASTAN (Geometry view and Database manager)

- **Reaction 1:**



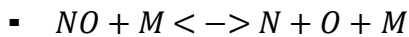
where the reactants =  $N_2$ ,  $M$  and the products =  $2N$ ,  $M$

- **Reaction 2:**



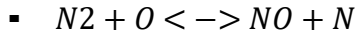
where the reactants =  $O_2$ ,  $M$  and the products =  $2O$ ,  $M$

- **Reaction 3:**



- where the reactants =  $NO, M$  and the products =  $N, O, M$

- **Reaction 4:**



- where the reactants =  $N_2, O$  and the products =  $NO, N$

- **Reaction 5:**



- where the reactants =  $NO, O$  and the products =  $O_2, N$

- **Physics Setup:**

- Compressible Flow, Reacting/Mixing Fluids, Axisymmetric, Inviscid (Euler), Two Temp. Non-Equilibrium, Reacting (Finite Rate), Time-Accurate, Linear Ramp, Roe's Flux-Difference Splitting, First Order, Backward Euler, Implicit

- Initial Conditions

- Flow

- Velocity (x-direction) = 7000 m/s

- Velocity (y-direction) = 0 m/s

- Static Pressure = 5.25 Pa

- Static Temperature = 219.7K

- Chemistry

- Temperature (Internal) = 219.7K

- Mixture =  $NO, N, N_2, O, O_2$

- Boundary Conditions

## Inflow/Outflow

Velocity (x-direction) = 7000 m/s, Velocity (y-direction) = 0 m/s, Static Pressure = 5.25 Pa, Static Temperature = 219.7K

## Chemistry

Temperature (Internal) = 219.7K, Mixture =  $NO, N, N_2, O, O_2$

## Outlet

Extrapolated pressure

## Wall (Command Module)

Heat transfer = adiabatic, Flow condition = no-slip

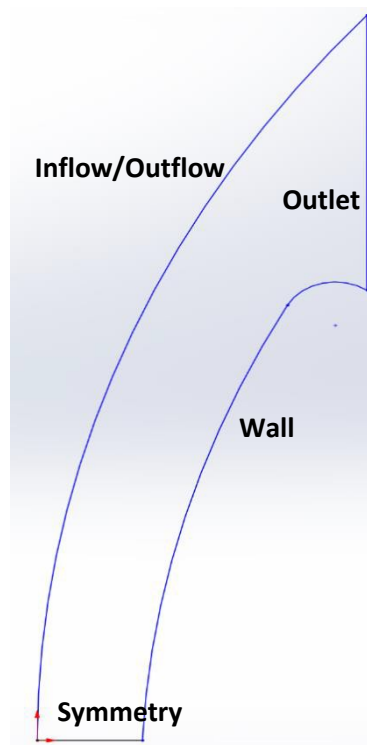


Figure 14. Boundary conditions

The simulation was run for 5,000 cycles with a timestep size of one second. In later sections, it will show in the results that 5,000 cycles were not enough to reach convergence and that it took longer than expected. It will be discussed later, ways to improve on reaching convergence with less cycles, but with the same quality of the solution, meaning no loss in its accuracy.

# Chapter 3

## Post Analysis

### 3.0 Results

During the simulation, it was discovered that 5,000 cycles were too low to reach convergence and that may have been due to either the physics setup or the model of the chemical reactions. However, the simulation eventually reached convergence after running enough cycles of about 140,000. The residual level on the residual plot were more than acceptable to agree that convergence was reached even if it didn't flatten out to a constant value like it did in this simulation. Even though there is clear evidence of convergence in this simulation, for its purposes, it was only done to initialize both the mesh and the entire setup of the physics. These results are not of high-fidelity or using conditions from research work, the conditions and setup parameters used in this simulation were from the tutorials of CFD-FASTRAN. However, the geometry is different, therefore number of cycles to reach convergence are different since physics and the chemical reactions occur differently due to a different geometry. Below is a plot of the residuals including the results which show the mass fractions of each gas.

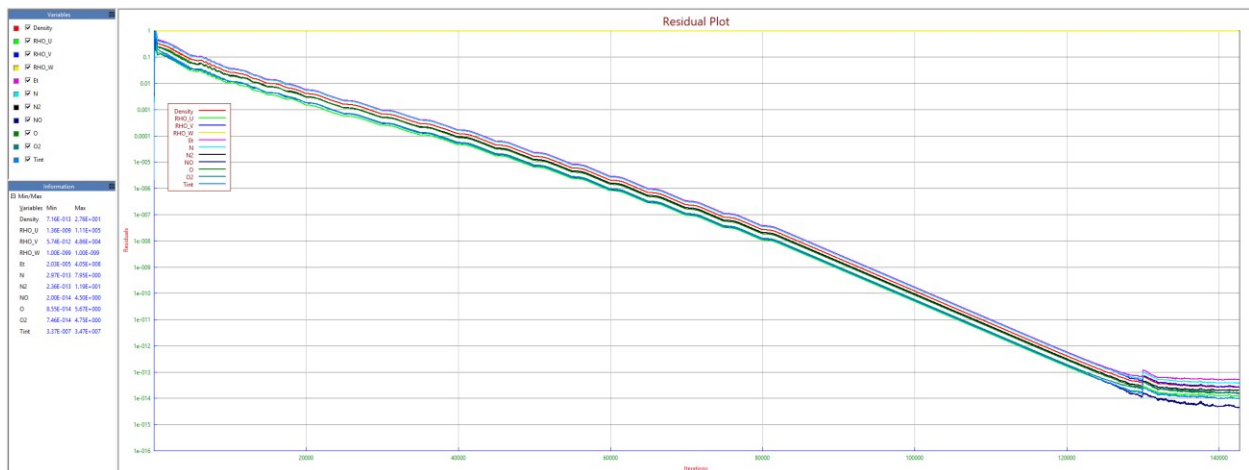


Figure 15. Residual Plot (~140,000 cycles)

It can be seen that the residuals start to flatten out and convergence is reached a little under 140,000 cycles with residual levels leveling out between of  $1 \times 10^{-12}$  and  $1 \times 10^{-13}$ . There are a

few oscillations at the initial stages of the simulation and towards the end where convergence is reached, but those are normal and to be expected in supersonic/hypersonic cases. The next couple of figures displayed below are mass fractions of  $NO$ ,  $N$ ,  $N_2$ ,  $O$ , and  $O_2$ .

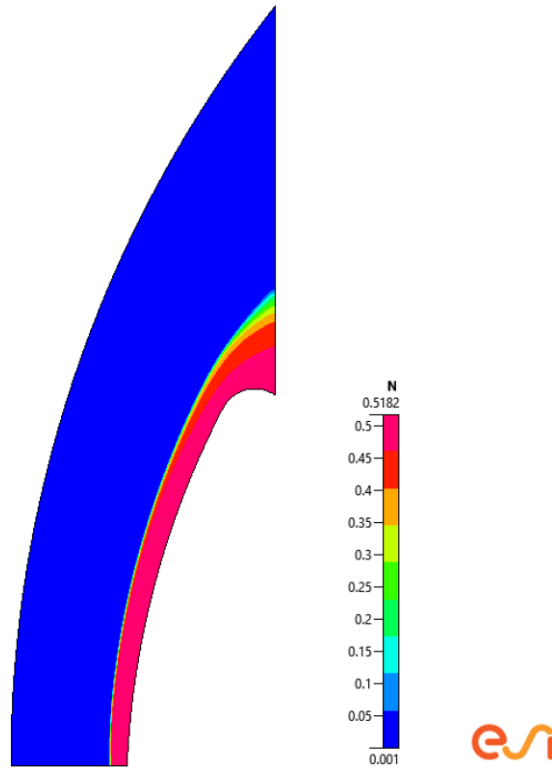


Figure 16. Mass fraction of N

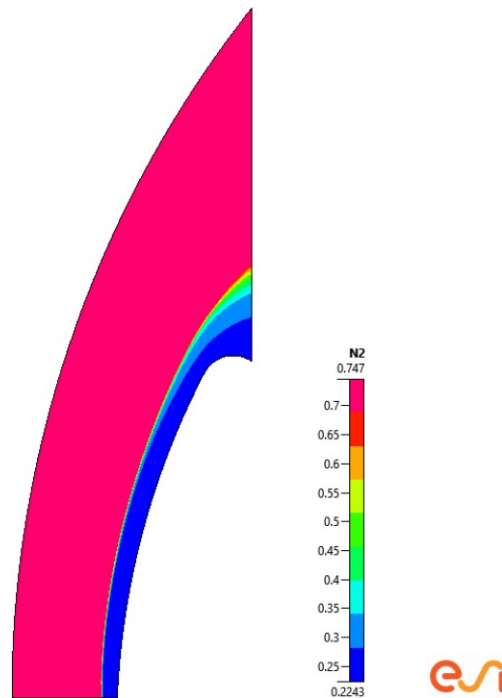


Figure 17. Mass fraction of N2

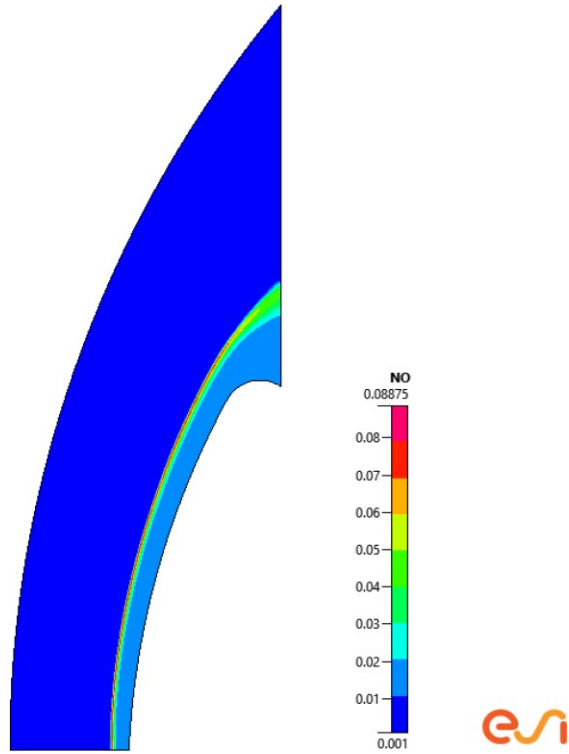


Figure 18. Mass fraction of NO

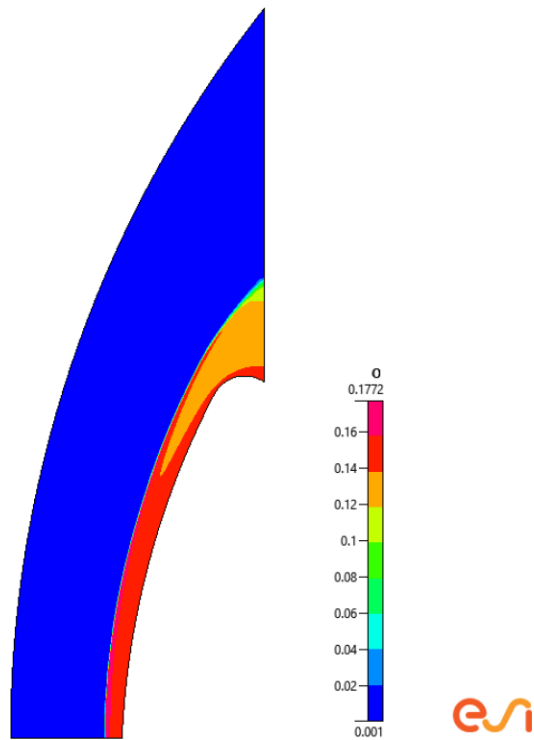


Figure 19. Mass fraction of O

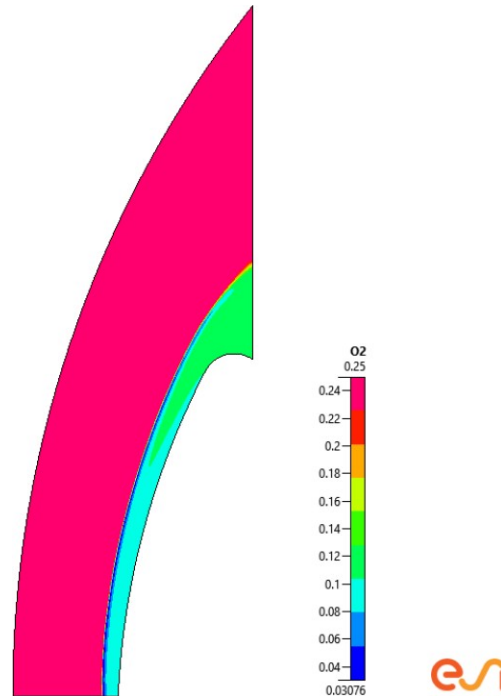


Figure 20. Mass fraction of O2

The results of the mass fraction are only slightly higher compared to those from the tutorial's results which is mostly likely due to a different geometry (round bluff body v. command module). However, seeing that the mass fraction between the tutorial and the ones generated from this simulation difference is under 5%, that is very acceptable and could be observed as high-fidelity since this initialization setup did reach convergence. Moving forward with future simulations, there will be high-fidelity results of other simulations done on a similar geometry.

### **3.1 Discussion**

With the initial setup of the simulation reaching convergence, this is good moving forward in creating high-fidelity results with other research work on a similar geometry to the command module. This will allow for quicker debugging when simulating various sets of conditions from other works. Even though there was convergence, it can be improved on with a better physics setup and models for the chemical reaction with conditions from works of a similar geometry. The focus for future simulations will just be the solver setup, but the geometry will matter as well, so the only ones conducted on the command modules (AS-202) which can be found in AIAA – Journal of Thermophysics and Heat Transfer. Also, considering works done with NASA codes such as DPLR (Data Parallel Line Relaxation) will prove to be most helpful in creating high-fidelity results.

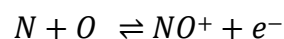
# Chapter 4

## Radio Attenuation Measurement (RAM)

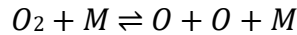
### Project

#### 4.0 Project RAM

Project RAM was a project conducted at NASA Langley during the mid-to-late sixties and so on. The objective of the project was to study the effects of the re-entry plasma on the communications systems of the vehicle upon re-entry. This project conducted both theoretical and experimental studies which included eight rocket flights. Out of the eight rocket flights (1961 – first flight), seven were successful in gathering the data necessary for these studies. The re-entry speeds for these successful flights were 5.5 km per second for the first four and 7.5 km per second for the last three. One of these flights were the RAM A-I and RAM A-II, with objectives that included determining the effectiveness of techniques like aerodynamic shaping and magnetic windows in mitigating the communications blackout problem. Both the RAM A-I and RAM A-II were successful in achieving the mission objectives, by making signal attenuation and antenna impedance measurements to help determine the effectiveness of the techniques. The results (Sims and Jones, 1962-1963) from both flights however, are classified and not available in open literature. The other flights were the RAM B-I and RAM B-II, with RAM B-I designed for a series of missions of radio attenuation experiments for multiple frequencies. However, the RAM B-I rocket was not successful due to a technical malfunction. For the RAM B-II rocket, its main mission was to experiment with the use of water injection to observe its effectiveness to the re-entry plasma in mitigating the communications blackout problem. The flight of the RAM B-II was successful, and the data did show that the addition of water was able to alleviate some of the problems caused by the re-entry plasma, but only to a degree. Quantitative data from the RAM B-II experiment is however, remains in classified literature (Cuddihy, 1963-1967). After flights RAM B-I and RAM B-II, the RAM B-III rocket was prepped for a mission that would be to study the antenna impedances of the VHF, X-band, and S-band during re-entry. The data gathered during the RAM B-III mission was to help in studying the properties of the re-entry plasma sheath. The measurements from the flight was able to confirm some predictions made on the properties of the re-entry plasma. One of it being on the dominant ionizing reaction as follows:



which occurred at altitudes of 40 to 50 km at velocities of 6 km per second. Another prediction was on the temperature range on the rate coefficients for the above reaction, with a range of 3000 to 7000 K to which the predictions were within a factor of two regarding the rate coefficients. It was also predicted that the following reaction:



that the impedance of the antenna would be sensitive to the rate of coefficient to the above reaction in low altitudes and low velocities. Both the experimental measurements and calculations done in the predictions, resulted in the temperature range for the rate coefficient for the dissociation of oxygen, that being 4000 to 6000 K. Quantitative results and discussions from the RAM B-III flight are in classified reports (Graham, Evans, and Schexnayder, 1964-1967).

After the flights of the RAM B-I and RAM B-II rockets, the RAM C-I and RAM C-II rockets were the next set of iterations that would be used to further measure and study the properties of the re-entry plasma sheath. The RAM C-I rocket was similar to the RAM B-I, in which water was to be injected into the plasma flow during re-entry to study its effectiveness on mitigating it. Not only did it inject fluid into the re-entry plasma sheath, RAM C-I was equipped with the electrostatic probes that were used to measure the density of the ions and its distribution in the flow field and along the rocket, but more so at the nose which was the stagnation point. There were other measurements that were made during re-entry, microwave signal attenuation and antenna impedance measurements, to measure the effectiveness of the water injection. According to post-analysis from these experiments, the addition of water was not effective to the degree as predicted in reducing the effect of the communications blackout problem (Cross and Akey, 1970). The next flight, RAM C-II, was equipped with electrostatic probes to determine the ion density and its distribution in the flow field, similar to the RAM C-I. Other equipment on the RAM C-II vehicle was used to measure the electron density of the re-entry plasma layer including its standoff distance (Jones, Cross, and Graham, 1970). The figure (sub-divided into two) including the diagram below show the various nozzle configurations of the orifices used in the liquid injecting techniques.

Nozzle patterns (a)	Disk	$D_j$ , cm	Liquid tested
Single orifice	1	0.0508	Water
Single nozzles of 1, 3, 5 or 7 orifices	1	0.0508	Water
Single rows of 1, 2, or 3 nozzles (5 orifices per nozzle)	1	0.0508	Water
Single rows of 4 or 5 nozzles (5 orifices per nozzle)	2	0.0508	Water
RAM C-III (low flow) ⑤ ● ●	1	0.0508	Water

RAM C-III (high flow) ⑤ ⑤ ⑤ ⑤ ●	2	0.0508	Water
RAM C-III (low flow) ① ③ ●	1	0.0508	Fluorocarbon
RAM C-III (high flow) ③ ⑤ ⑦	1	0.0508	Fluorocarbon
Nozzle pattern 1: ① ① ③ ① ① ③ ① ① ③	1	0.0254, 0.0508	Water, Fluorocarbon
Nozzle pattern 2: ⑤ ⑤ ⑦ ⑤ ⑤ ⑦ ⑤ ⑤ ⑦	1	0.0254, 0.0508	Water
Nozzle pattern 3: ① ① ● ● ● ● ① ① ●	2	0.0508	Water, Fluorocarbon
Nozzle pattern 4: ⑤ ⑤ ● ● ● ● ⑤ ⑤ ●	1	0.0508	Water

Figure 21. Test nozzle patterns (Weaver 1972)

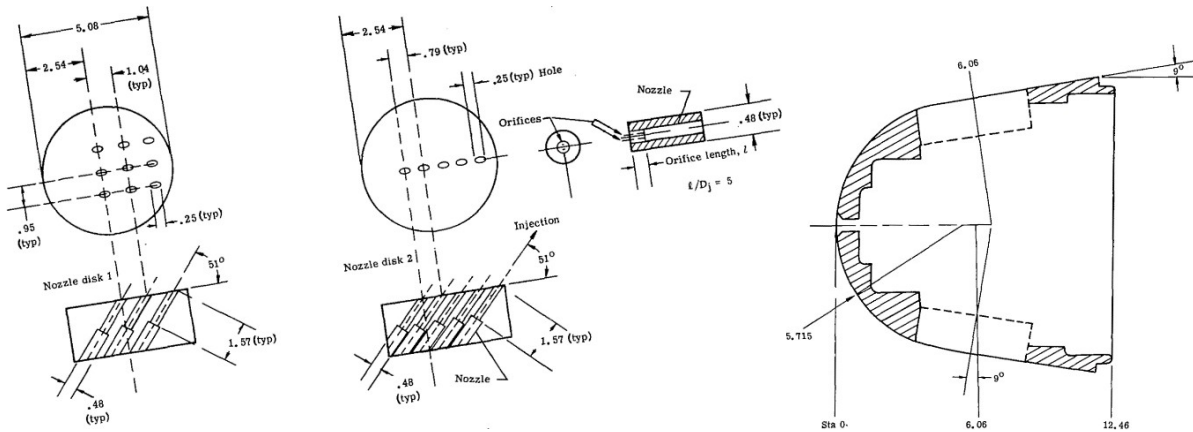


Figure 22. Nozzle disk assemblies (Weaver 1972)

The geometry for the RAM re-entry vehicles was a simple hemisphere-cone with a radius of 0.1525 m with a length of  $\sim 1.3$  m. The reason behind selecting a bluff body for the nose of the RAM was due to it being amenable to theoretical analysis. The experimental results from the flights were expected to be extrapolated either experimental or theoretical, to provide better estimates on the communications blackout problem. The results were extrapolated, then used in creating techniques for mitigating re-entry plasma effects for more intricate space vehicle

designs. The following figures below are the design and geometry schematics of the RAM vehicles (incl. launch vehicle) used in the RAM development and project program. Project RAM was considered successful in expanding the knowledge base on the communications blackout problem including the properties of the re-entry plasma sheath and the effects of various techniques in mitigating it.

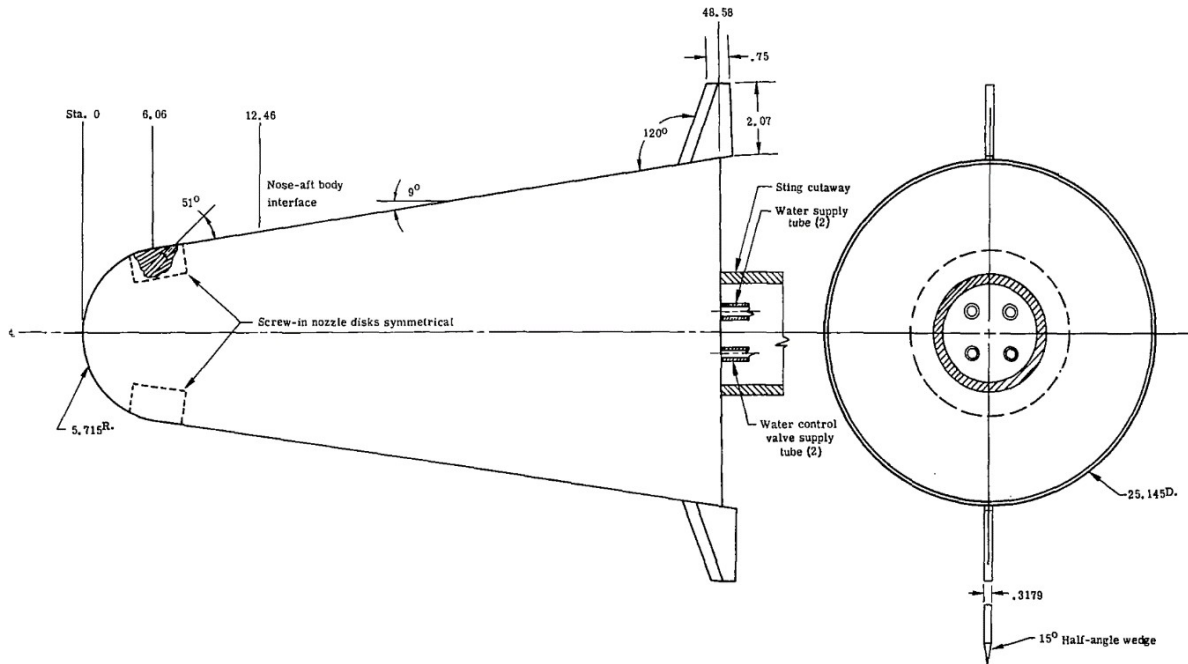


Figure 23. RAM C-II test model (Weaver 1972)

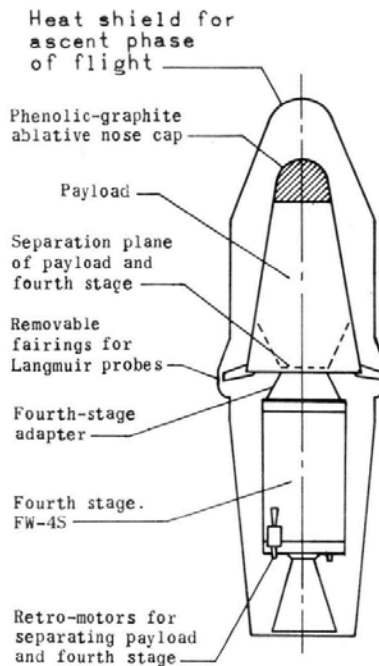


Figure 24. Spacecraft (Weaver 1972)

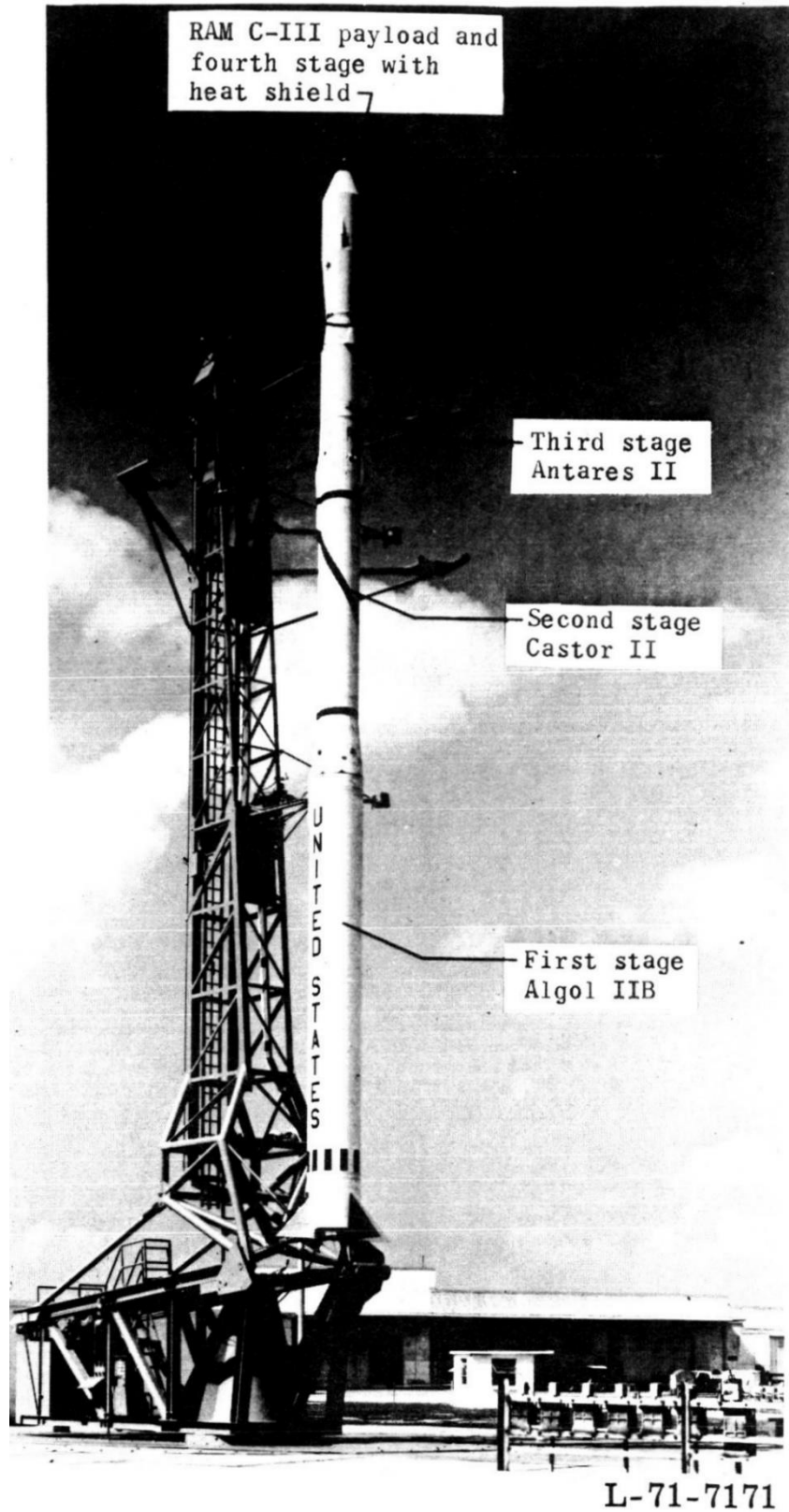


Figure 25. Boost vehicle (1972)

The results and data from the RAM project – especially those that are unclassified, have been used widely by researcher scientists for years in an effort in trying to mitigate the communications blackout problem. The RAM project has also become a great source of reference in furthering the understanding on the properties of the re-entry plasma sheath. For that reason, the work conducted for this report are based off the work done using data from Dr. Chul Park (Reaction Flows Branch – NASA Ames Research Center) as well as CFD analysis conducted by Candler and MacCormack. Both Candler and MacCormack reference Park in most of their work regarding reacting flows. Park is a very well-known research scientist who has worked in the space shuttle program and also for his many reaction models that represent the chemistry that occurs during re-entry. In the following chapters and sections, will include the simulations based on Candler, MacCormack, and Park’s works in analyzing the reactions in high-speed flows.



# Chapter 5

## Advanced Validation of CFD using a Navier-Stokes Solver

### 5.0 Weakly Ionized Hypersonic Flows

A numerical method developed by MacCormack and Candler used to compute a two-dimensional hypersonic flow field including an analysis which validated results from experiments conducted by Park in his work on reacting flows in hypersonic flow fields. The parameters and boundary conditions of MacCormack and Candler's work – Computation of weakly ionized hypersonic flows in thermal nonequilibrium (incl. other papers), were taken in conducting this analysis that would validate the results achieved. The solvers in both present and referenced work (MacCormack, Candler 1991) are different and uses various techniques in resolving the flow field, however, both solve the same underlying equations that govern the flow. Similar to the previous simulations conducted in the present work, FASTRAN was used to perform the simulations in validating the referenced work (MacCormack, Candler 1991). There are, however, some discrepancies that will need to be investigated further to find out what conditions that could be the reason for it.

The coupled equations were solved using the numerical method that based on the implicit Gauss-Seidel line relaxation technique which is greatly discussed by MacCormack and Candler's previous works (MacCormack, Candler 1987) (MacCormack 1985) (MacCormack, Candler 1987). The fully coupled equations that represent a hypersonic flow field are described by partial differential equations for which were solved to obtain a steady-state solution. The steady-state solution in the referenced work (MacCormack, Candler 1991) was obtained for a gas consisting of seven species ( $N_2$ ,  $O_2$ ,  $NO$ ,  $NO^+$ ,  $N$ ,  $O$ ,  $e^-$ ) characterized by six temperatures (one vibrational temperature per diatomic species for four total, electron temperature, and one translational-rotational temperature). Their computed results on the flow field of the sphere cone – based on the RAM vehicle, were in good agreement with experimental results from the RAM C-II flight experiment. The governing equations that describe the computed flow field are the conservation of species mass, vibrational energy, total energy, mass-averaged momentum, and electron energy are listed below:

- Mass conservation of the species:

$$\frac{\partial \rho_s}{\partial t} + \frac{\partial(\rho u)}{\partial x_j} = - \frac{\partial(\rho_s v_{sj})}{\partial x_j} + w_s \quad (8)$$

- Mass-averaged momentum:

$$\frac{\partial(\rho u_s)}{\partial t} + \frac{\partial(\rho u_i u_j)}{\partial x_j} = - \frac{\partial(\tau_{ij})}{\partial x_j} + \sum_s e_s N Z_{s s i} E \quad (9)$$

- Vibrational energy:

$$\frac{\partial E_{vs}}{\partial t} + \frac{\partial(E_{vs} u_j)}{\partial x_j} = - \frac{\partial(E_{vs} v_{sj})}{\partial x_j} - \frac{\partial q_{vsj}}{\partial x_j} + Q_{\tau-us} + Q_{v-us} + Q_{e-us} + w_{s vs} \quad (10)$$

- Electron energy:

$$\frac{\partial E_e}{\partial t} + \frac{\partial[(E_e + \rho_e) u_j]}{\partial x_j} = - \frac{\partial[(E_e + \rho_e) v_{ej}]}{\partial x_j} - \frac{\partial q_{ej}}{\partial x_j} - \frac{\partial[(u_i + v_{ei}) \tau_{eij}]}{\partial x_j} + N_e e \tilde{E}_i (u_i + v_{ei}) + Q_{\tau-e} - \sum_s Q_{e-us} + w_{e e} \quad (11)$$

- Total energy:

$$\frac{\partial E}{\partial t} + \frac{\partial[(E + \rho) u_j]}{\partial x_j} = - \frac{\partial(q_j + q_{vj} + q_{ej})}{\partial x_j} - \frac{\partial(u_i \tau_{ij})}{\partial x_j} - \frac{\partial}{\partial x_j} \sum_s v_{sj} \rho_{hs} + \sum_s e_s N Z_{s s i} E u_{si} \quad (12)$$

With the flow field of the problem defined by the equations above, next was defining the boundary conditions for the problem. The freestream was set to supersonic as it should with all the variables made known. The outlet is also set to supersonic, setting the exit condition with a zero gradient. The wall (RAM) was assumed to be adiabatic, so no heat flux and set to have a no-slip condition. There were no surface reactions at the wall, therefore, the wall was assumed to be noncatalytic, meaning at the wall, the mass fractions of the species was zero. However, in Park's work – frequently referenced by Candler and MacCormack, finite-rate catalytic recombination of the atoms could be included using expressions developed by Park. Also, adding a perfectly catalyzed electron-ion recombination reaction to the wall boundary condition, would be more accurate. Now that both the flow field and its boundary conditions have been defined, the geometry and the mesh were generated. The geometry was a hemispherical cone, taken from the RAM project vehicles, and was simplified to not include negligible details like fins along with other external protrusions that wouldn't benefit the results of the computation. The mesh

generated was rather coarse mesh by today's standards regarding mesh quality leading to a quality solution. The generated grid was structured with dimensions of 35 by 50, with a total cell count of 1,666 cells and 1,750 nodes which can be seen in figure X below.

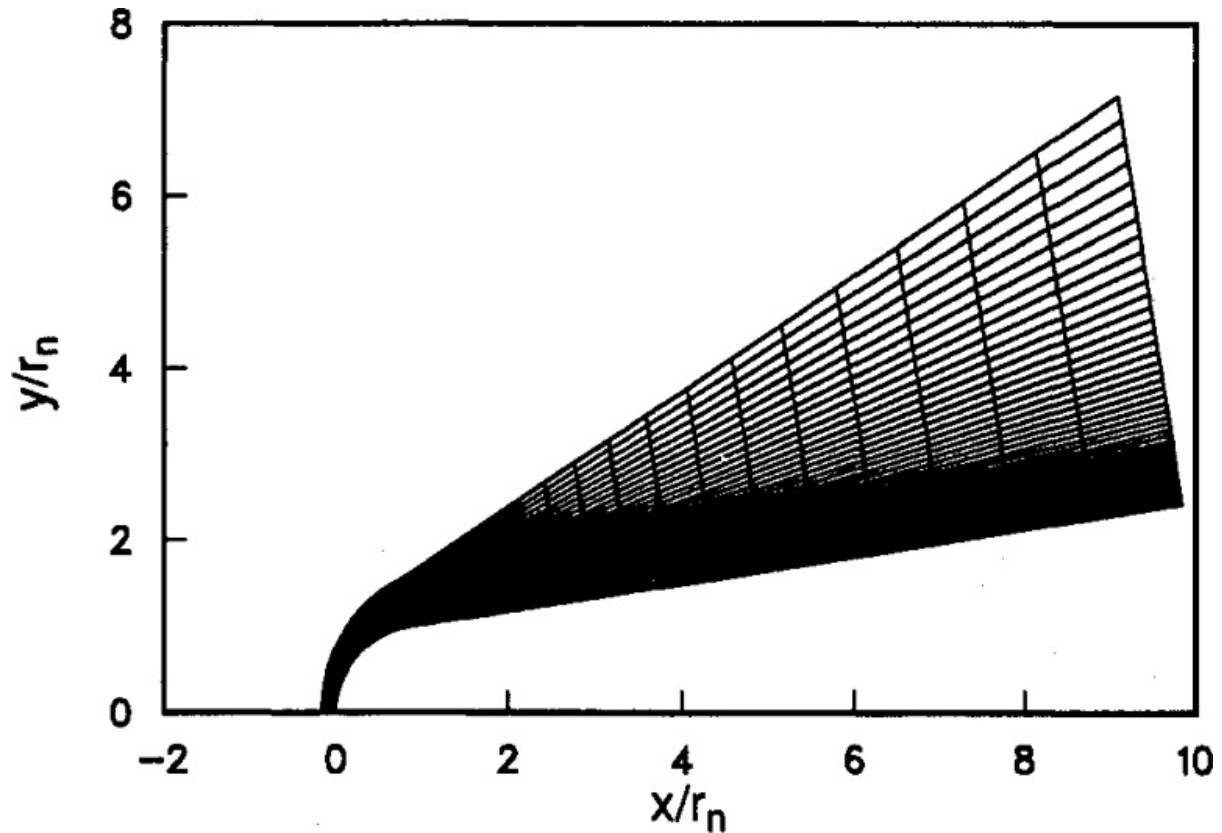
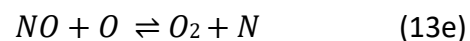
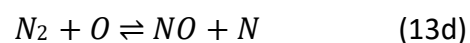
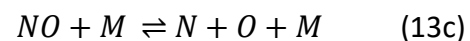
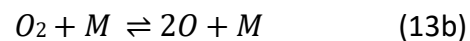
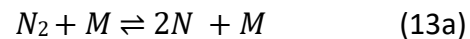
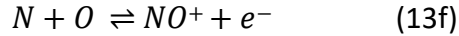


Figure 26. 35 x 50 grid (MacCormack, Candler 1991)

On the chemistry aspect of the problem, the chemical reactions of the seven species considered are as follows:





where M is a third body in the reaction and represents any of the seven species. The third body is a requirement in third body reactions since it stabilizes the excited product(s) by collision. The third body removes any of the excess energy from the product(s) which as some point will dissipate it as heat. This reaction model including its parameters were experimentally determined by Park (Park, 1985) (Park, 1986) (Park, 1987).

With the problem defined with all of the different aspects to correctly represent the flow field, the flow was computed to replicate the RAM C-II experiments at various altitudes of 61, 71, and 81 km. These three cases were simulated for the RAM C-II geometry which was described in the previous chapter with dimensions measuring at 0.1524 m nose cone radius, a 9 degree cone half angle, and a total length of 1.3 m. During the RAM C-II experiments, the electron densities were measured at four locations with the use of a microwave reflectometers as well as an electrostatic rake in the boundary layer. The cases were simulated with conditions of the freestream shown in the table below. The altitude range that the computations were performed, were approximately ranging from states of thermal equilibrium to thermal nonequilibrium. An approximation of the wall temperature was set as close as possible to actual, which was fixed at 1000 K. Since there were no surface reactions included in the simulation, the wall was assumed to be noncatalytic. The velocity of the freestream was set to 7650 m/s for all three cases with the freestream composed of 79%  $N_2$  and 21%  $O_2$ .

**Table 1 Freestream conditions for computed cases**

Altitude, km	$M_\infty$	$Re$
61	23.9	$1.95 \times 10^4$
71	25.9	$6.28 \times 10^3$
81	28.3	$1.59 \times 10^3$

Figure 27. Freestream conditions (MacCormack, Candler 1991)

The results of the simulations show that it was very close to those from the experiment. The plots in the figures below show comparisons with the experiment regarding the electron number density, which was found in both cases to be greatest at the stagnation point, that being the at the nose. Each of the plots represent and compare the electron number density measurements axially along the body for each of the three altitudes. Density of the electron number is at its peak at the nose and decreases rapidly along the body towards the shoulder. A large number of free electrons are produced at the nose during the gas reactions, have not yet been recombined, are carried by the flow along the body.

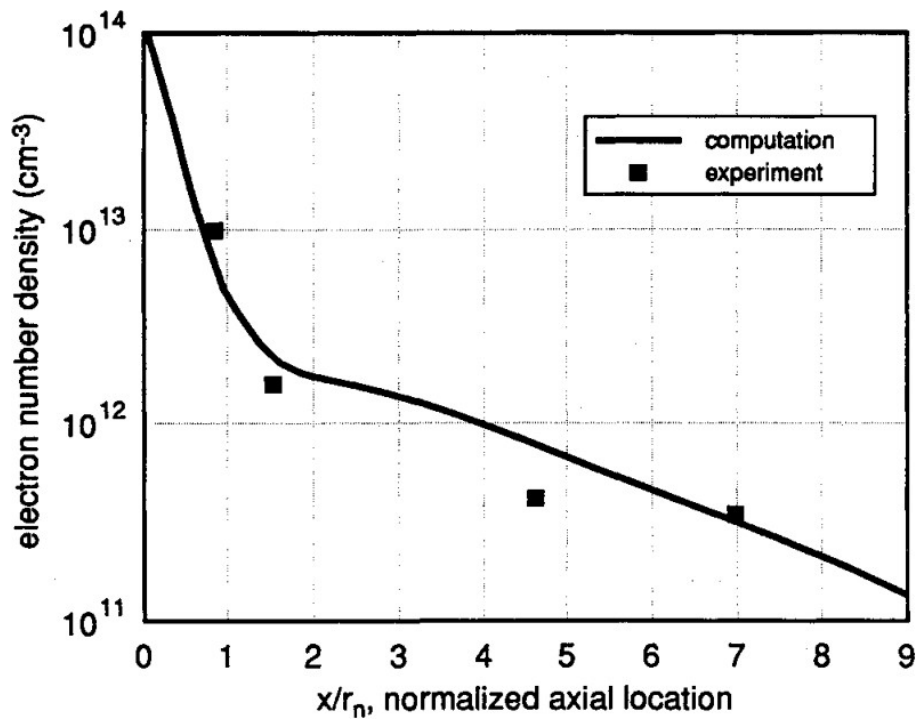


Figure 28. Peak electron density comparison, 61 km (MacCormack, Candler 1991)

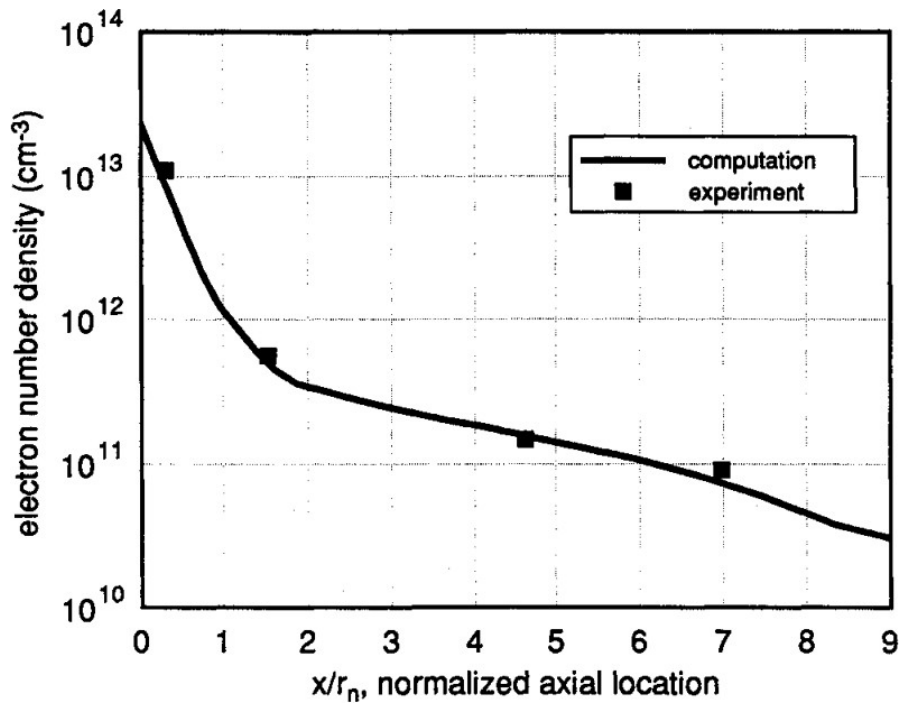


Figure 29. Peak electron density comparison, 71 km (MacCormack, Candler 1991)

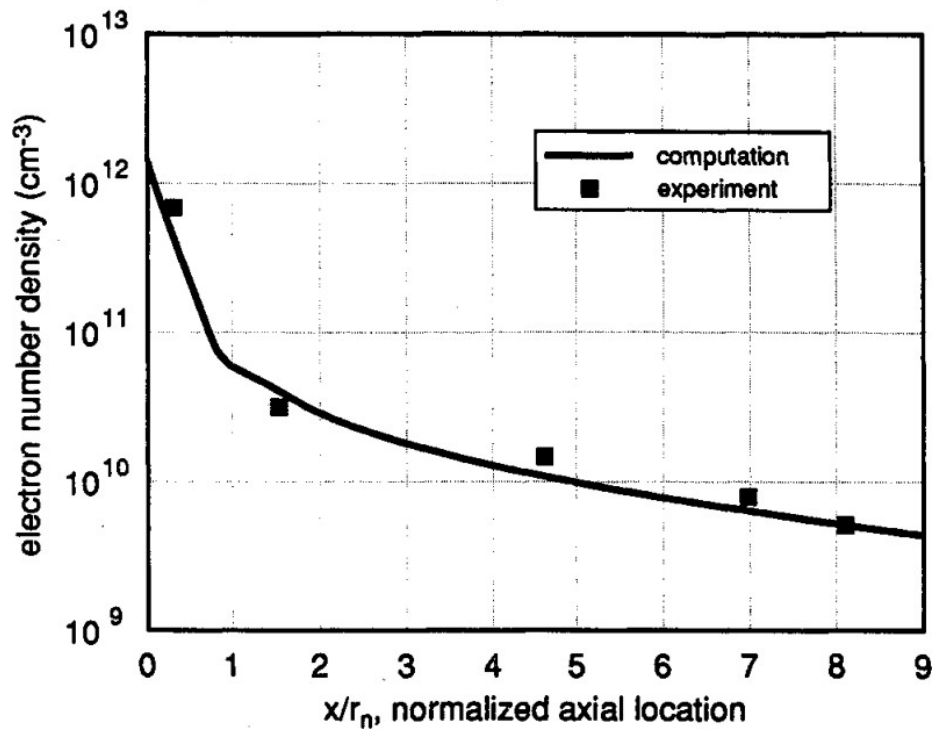


Figure 30. Peak electron density comparison, 81 km (MacCormack, Candler 1991)

The next set of plots in the following figures below show the mass fractions of the major species of the reacting gases at the stagnation point. To a degree, these plots indicate whether or not there is thermal nonequilibrium in the flow field for each of the cases being simulated. Mentioned earlier was a suggestion by Park, that having a wall boundary condition that was fully catalytic for the electron-ion recombination might have some effect on the peak electron mole fraction. However, the results show that even in the inviscid region, there is a peak of the electron mole fractions. This would mean that having a wall boundary condition being fully catalytic, would have been ineffective in changing the comparison to the RAM project experiments, that being the RAM C-II experiment.

The other figures are plots that display a few of the flow field quantities, which are contours of the translational, rotational, and vibrational temperatures of  $N_2$ . All three temperatures of  $N_2$  are the same in distribution regarding the peak values at the nose with a rapid decrease as the gas expands axially along the body and around the shoulder region. Although, there is some difference in the temperatures when looked at inspecting the contours closely. These temperature differences showcase thermal nonequilibrium within the flow field.

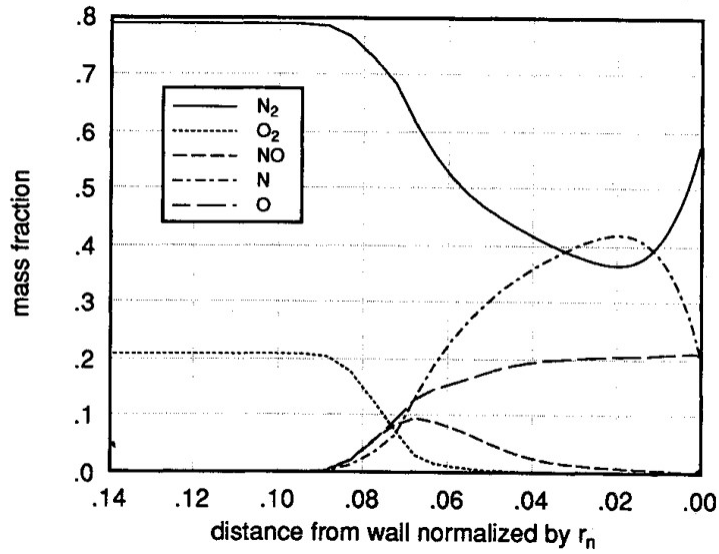


Figure 31. Mass fractions, 61 km (MacCormack, Candler 1991)

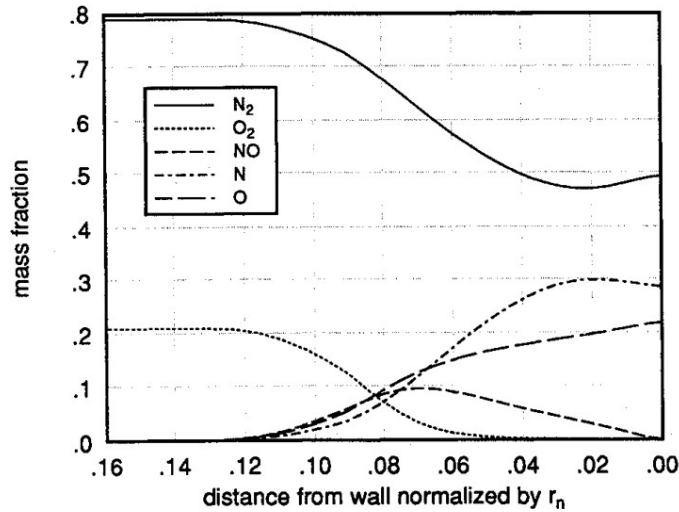


Figure 32. Mass fractions, 71 km (MacCormack, Candler 1991)

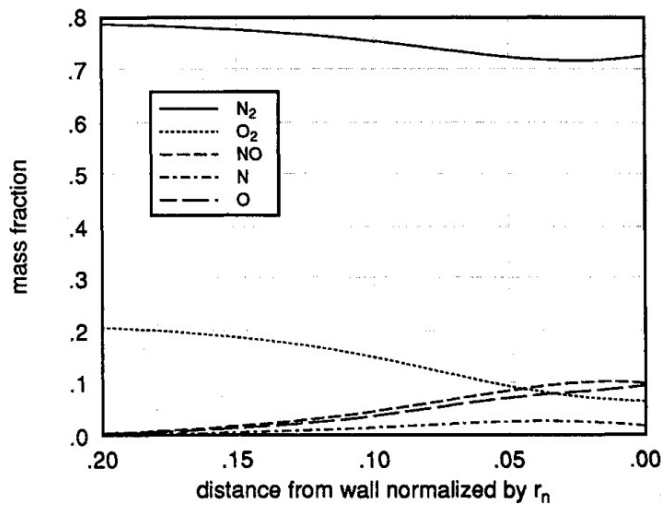


Figure 33. Mass fractions, 81 km (MacCormack, Candler 1991)

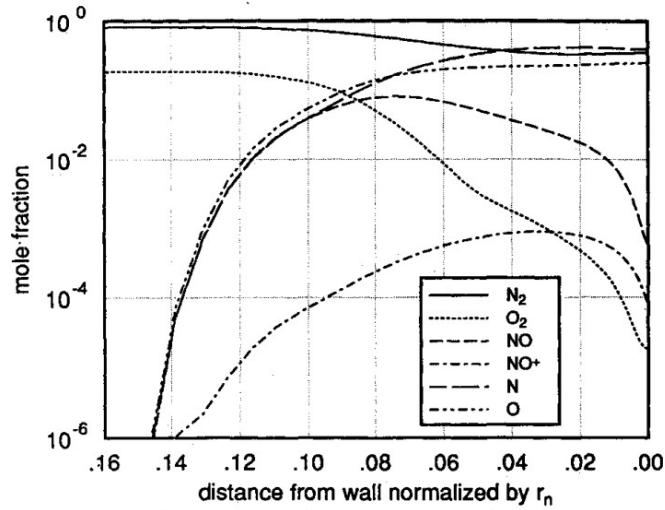


Figure 34. Mole fractions on stagnation streamline, 71 km (MacCormack, Candler 1991)

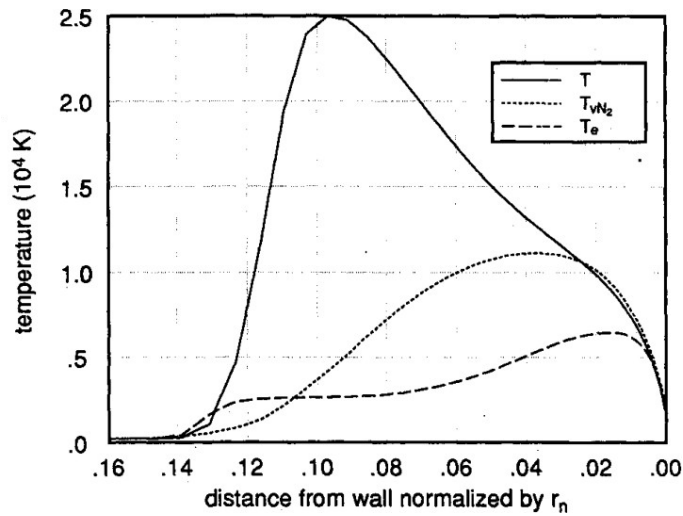


Figure 35. Temperature on stagnation streamline, 71 km (MacCormack, Candler 1991)

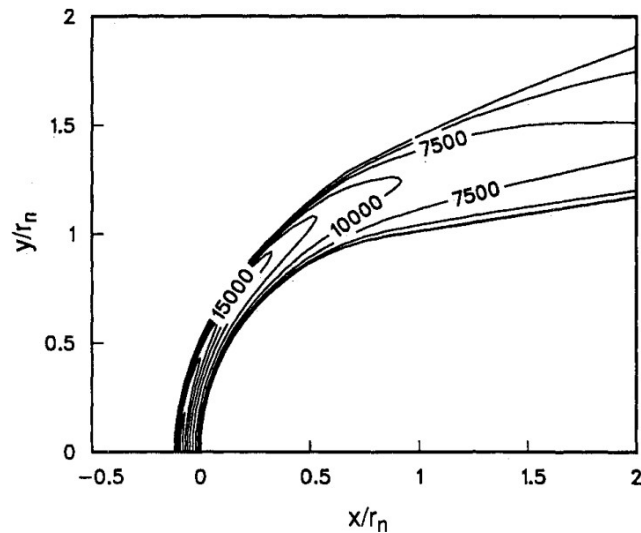


Figure 36. Contours of translational-rotational temperature (K), 71 km (MacCormack, Candler 1991)

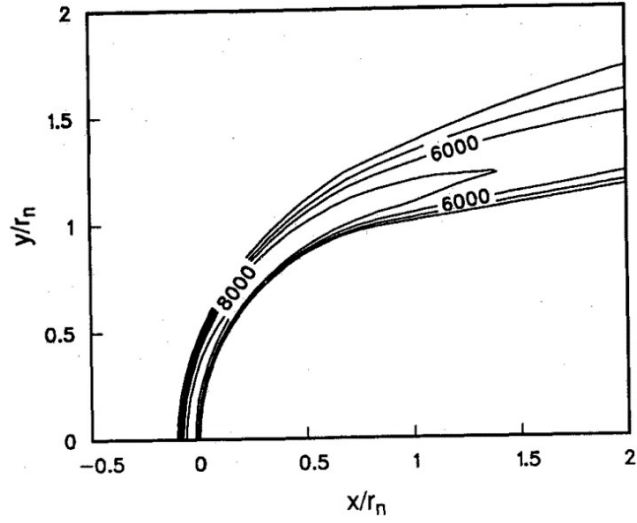


Figure 37. Contours of  $N_2$  vibrational temperature (K), 71 km (MacCormack, Candler 1991)

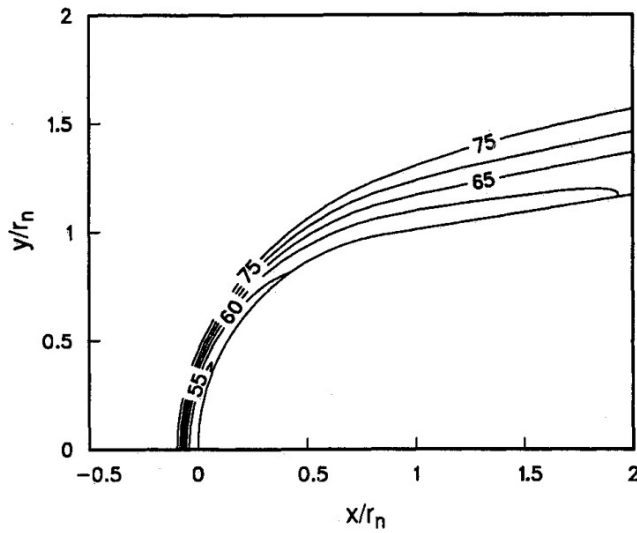


Figure 38. Contours of  $N_2$  mass fraction, 71 km (MacCormack, Candler 1991)

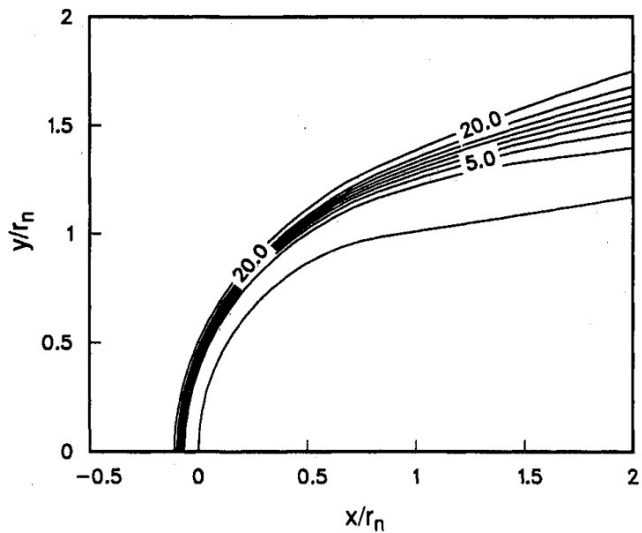


Figure 39. Contours of  $O_2$  mass fraction, 71 km (MacCormack, Candler 1991)

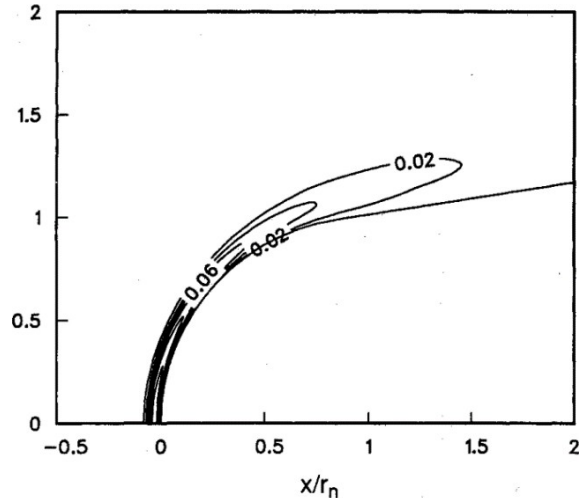


Figure 40. Contours of  $\text{NO}^+$  mass fraction, 71 km (MacCormack, Candler 1991)

In their work, a numerical method was developed for solving the fully coupled equations that describe a two-dimensional chemical thermal nonequilibrium of a hypersonic flow field. The high velocity and high temperature flow was modeled consisting of seven species characterized by six temperatures. Reviewing the results, it showed that the electron number densities from the computations were in very good agreement with the data from RAM C-II experiments. It was found from the simulation results, that a multitemperature model is required for describing the thermal state of the gases. However, describing and defining the flow field with a high accuracy requires a large set of equations, which makes getting the solution computationally intensive and expensive. Large iterations of the simulation were required due to the reaction rates being slower at higher altitudes compared to lower ones, because of the density. Also, it makes for solving the large set of equations numerically stiffer where the conditions are most complex. Although, the advantage of the method developed in this work makes it possible to model the reacting gas with additional species. Modeling for things like radiation or energy exchange mechanisms would not be possible, but also with high accuracy.

## 5.1 Validation Analysis

After reading MacCormack and Candler's work on the weak ionizing hypersonic flows, that information was then used to conduct a validation analysis especially using a solver – although commercial, would be a good indicator of robustness regarding the reactions model. Using a different solver in solving the same problem solved by MacCormack and Candler will also be a high-fidelity check. However, as mentioned earlier in this chapter, the solver (FASTRAN) used

for the validation analysis, no matter how different, it solves the same equations which govern and describe the flow field around a hypersonic vehicle or a hypersonic flow in general.

All of the parameters, if not, most of the parameters were used for the validation in modeling the flow field as close as possible to the referenced work (MacCormack, Candler 1991). The grid remained largely the same in terms of the number of cells and nodes, but the design of the grid was slightly modified in hopes of improving the solution which ended up not being the case. Other modifications to the setup of the validation process was on the chemistry aspect regarding third body efficiencies and the molecular properties for each of the species. Parts of the molecular properties that were modified include the molecular weight, degrees of freedom, collision diameter, etc. As for the chemical reactions, the reaction model used in the referenced work (MacCormack, Candler 1991) were experimentally determined in Park's previous work (Park 1985).

In the figures below, different iterations of the geometry were created using SolidWorks. There were several iterations showing the different designs of the flow field and the RAM C-II vehicle which is a similar process conducted on the previous simulations on the Apollo command module. Once the design of the geometry of the main body and flow field were completed, as always, the mesh or grid was generated using ESI's in-house CAD and mesh software package, CFD-GEOM.

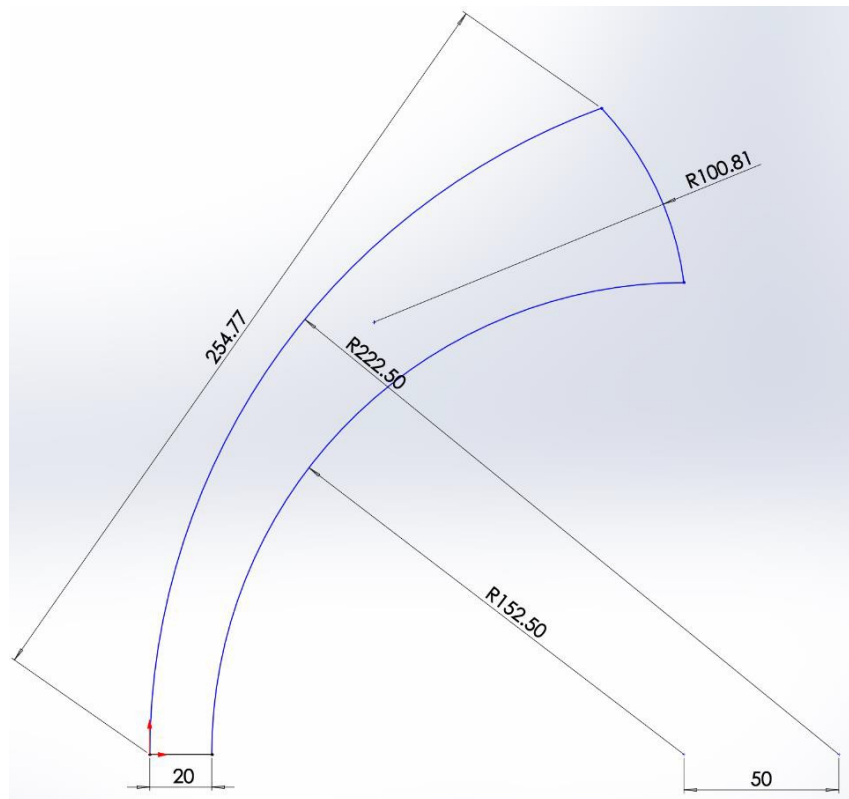


Figure 40. Design iteration 1.0

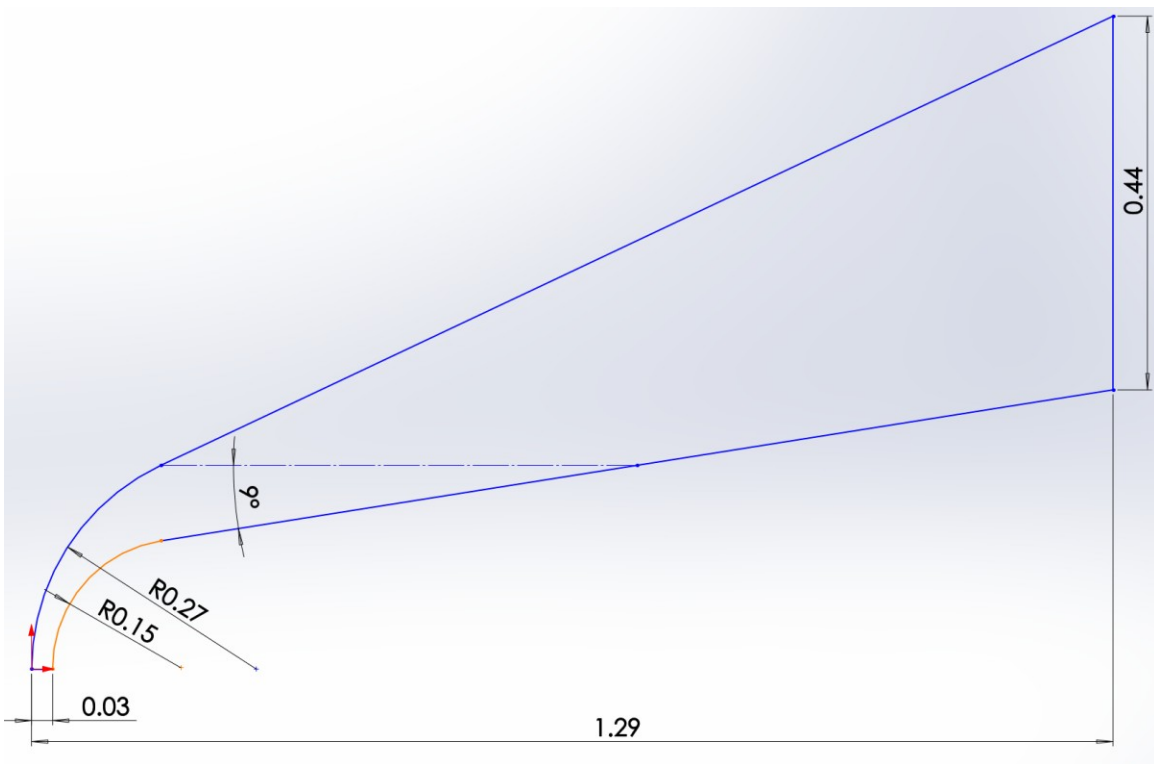


Figure 41. Design iteration 2.0

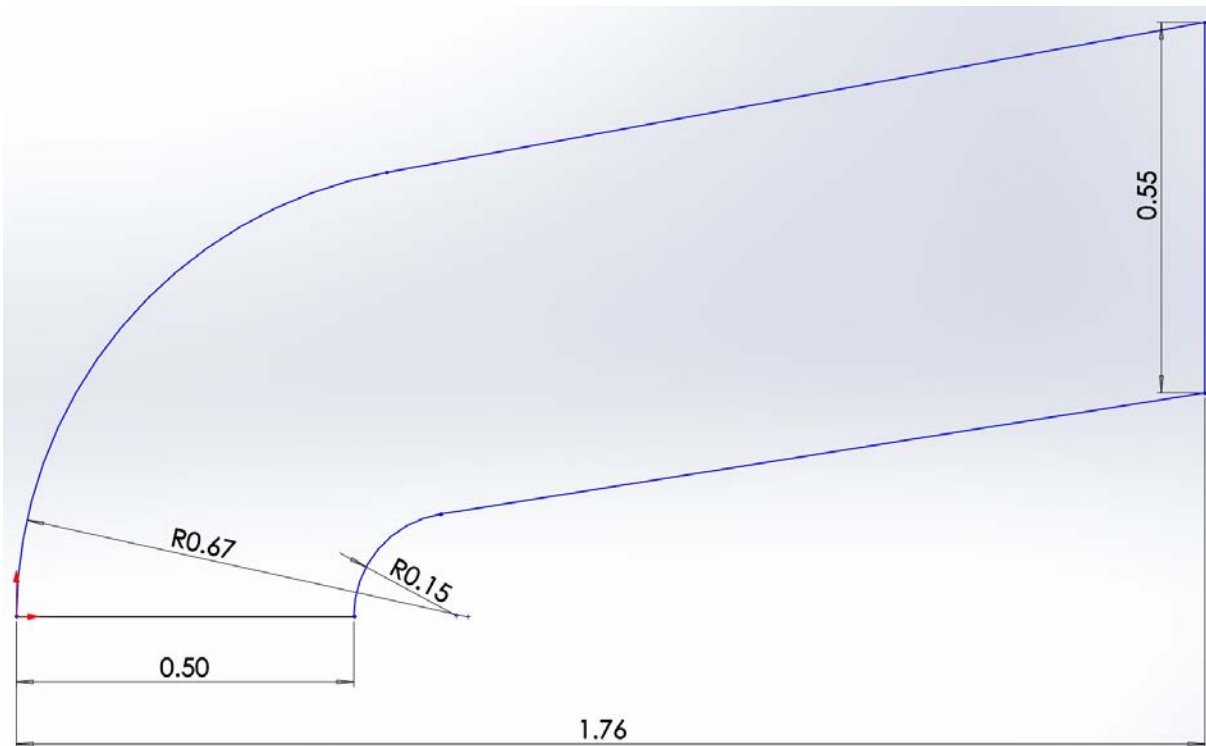


Figure 42. Design iteration 3.0

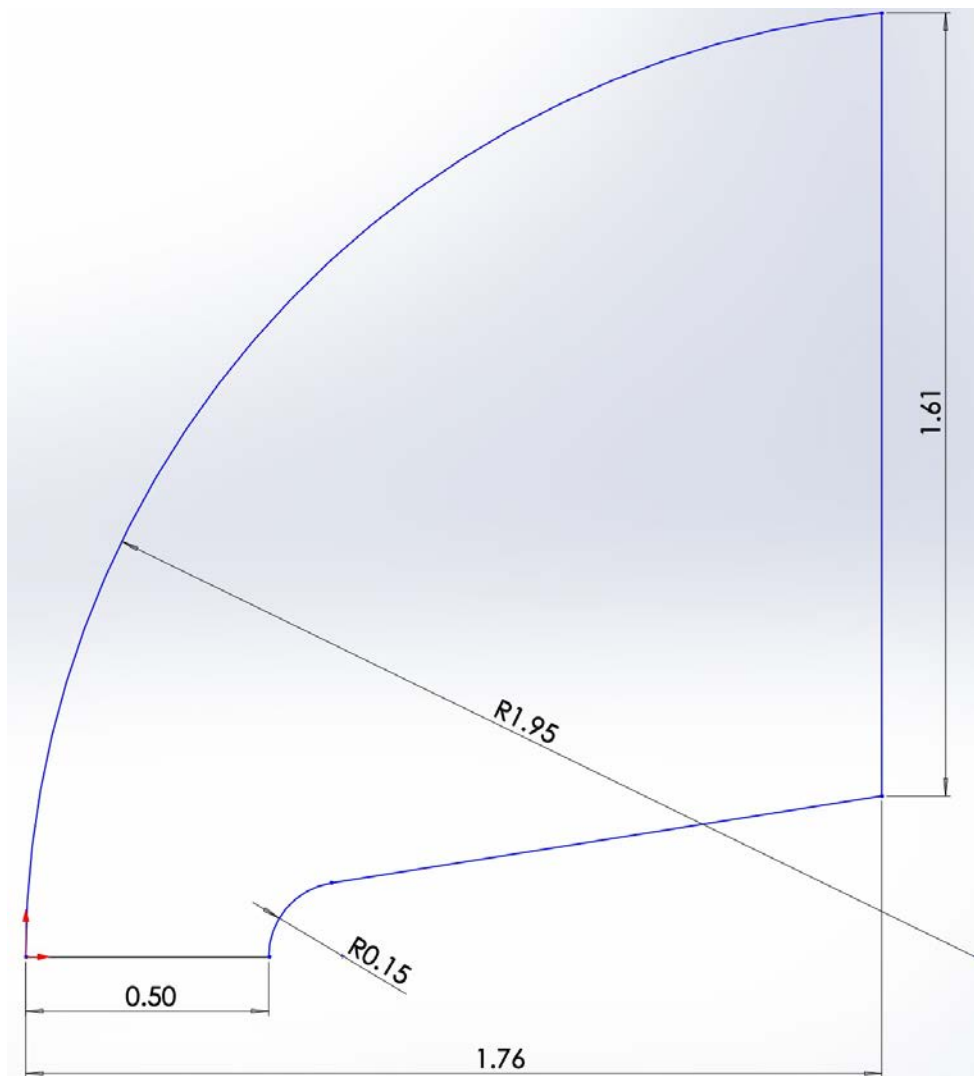


Figure 43. Design iteration 4.0

The design iterations above show the progress of the flow field and body's CAD design before the grid generation. Initially, the design was to be a replicant like the one used in the referenced work (MacCormack, Candler 1991), however, there some issues in simulation which caused the solution to diverge and the simulation to crash. These issues will be discussed in further sections. The first design was supposed to be a different approach where instead of wasting computing resources on any part of the body located past the nose, this design was supposed to enable for quicker simulations, while maintaining its accuracy. The last two design iterations worked in terms of converging to a solution, but the solution computed in the last design iteration was closer to the solutions computed in the reference work. The figures below show the grid for the last design iteration including the cell and node count.

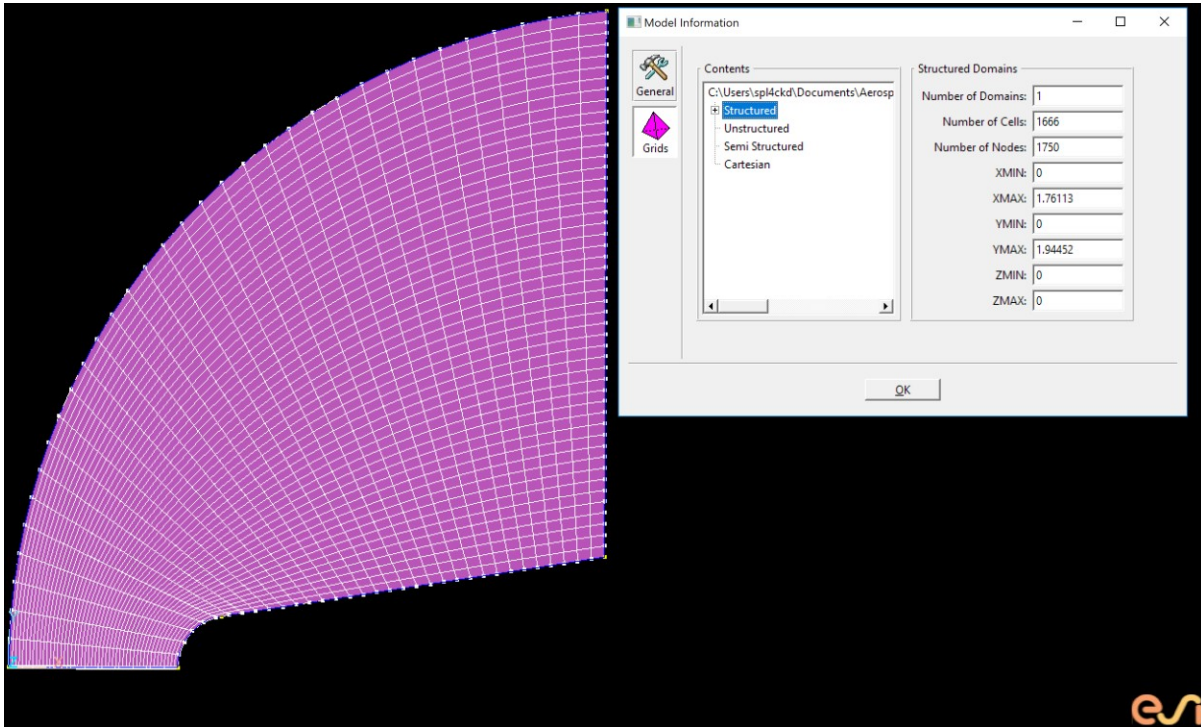


Figure 44. Coarse mesh – 35 x 50

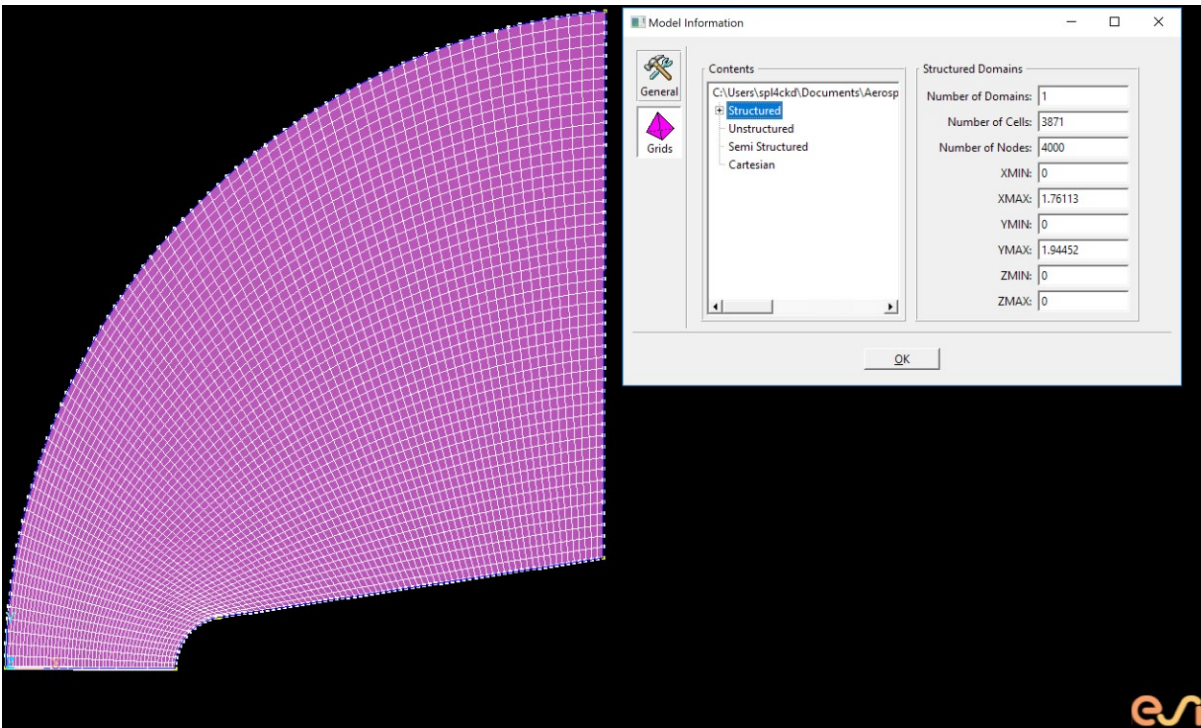


Figure 45. Fine mesh – 80 x 50

In the figure above, it shows the grid generation of the last and final design iteration. The dimensions of the grid were first set to the same dimensions in the referenced work (MacCormack, Candler 1991), however, that was only done to get a solution quickly using a coarse mesh. Once a converged solution was achieved, the mesh was refined mostly at the wall, in order to get a higher quality solution as well as to better capture the reactions in the flow field. The coarse mesh had an overall cell count of 1,666 cells and 1,750 nodes, which was later refined concluding with a total cell count of 3,871 cells and 4,000 nodes. The next step in the process show the chemistry settings for the species, mixture, and reactions. Since these settings used in this validation process are similar to that of the simulations for the Apollo module, a table should suffice in listing the parameters used. However, figures will still include some of the settings that might be less obvious.

Species	Mass Fraction
N <sub>2</sub>	0.79
NO	0
O	0
O <sub>2</sub>	0.21
C	0

Figure 46. Database manager – mixture settings for the species

The species model was the same as the one in the referenced work (MacCormack, Candler 1991), that being  $N_2$ ,  $O_2$ ,  $NO$ ,  $NO^+$ ,  $N$ ,  $O$ , and  $e^-$ . The same can be said for the species mixture, with its parameters shown in the figure above which models the gas composed of 79%  $N_2$  and 21%  $O_2$ . The next figure shown below displays the reactions which are volume reactions in the flow field.

No	Equation	Notes	Apf	nf	(Ea/R)f	Apb	nb	(Ea/R)b
1	$N_2 + M \leftrightarrow N + N + M$		1600000000	-1.6	113200			
2	$O_2 + M \leftrightarrow O + O + M$		2.9E+020	-2	59750			
3	$NO + M \leftrightarrow N + O + M$		7.95E+020	-2	75500			
4	$N_2 + O \leftrightarrow NO + N$		6.44E+014	-1	38370			
5	$NO + O \leftrightarrow O_2 + N$		8370000000	0	19450			
6	$N + O \leftrightarrow NO + E$		1530000000	-0.37	3200			

Figure 47. Database manager – chemical reactions

The data used in filling in the parameters for each of the reactions are from Park's previous works (Park 1985). The six reactions and reaction mode listed in the above figure were from the reference work including the species used. As for the molecular properties, the data was provided by the database located in FASTRAN and some were assumed using best educated guess including degrees of freedom and third body efficiencies. However, parameters such as collision diameter or characteristic energy for species like  $NO^+$ . These parameters can be considered further in future work when more simulation of other cases are conducted.

# Chapter 6

## Post Analysis

### 6.0 Results

All three cases were simulated, and the figures below are the results from the simulations. The results from the figures were generated by using the fine mesh in order to better visualize the quantities being analyzed. The computations were performed using the time accurate method which is transient along with a range of CFL (Courant-Friedrichs-Lewy condition) from 0.001 to 1 which was linearly ramped every thousand cycles. A total of 3,000 cycles were run for the simulation with a max time of 1 second. Higher order was selected for the spatial accuracy using the Osher – C limiter, both to increase the overall accuracy of the solution. The first few figures are the residual plots of each case, showing convergence for all three cases achieving a convergence within the residual range of  $1 \times 10^{-5}$  to  $1 \times 10^{-10}$ .

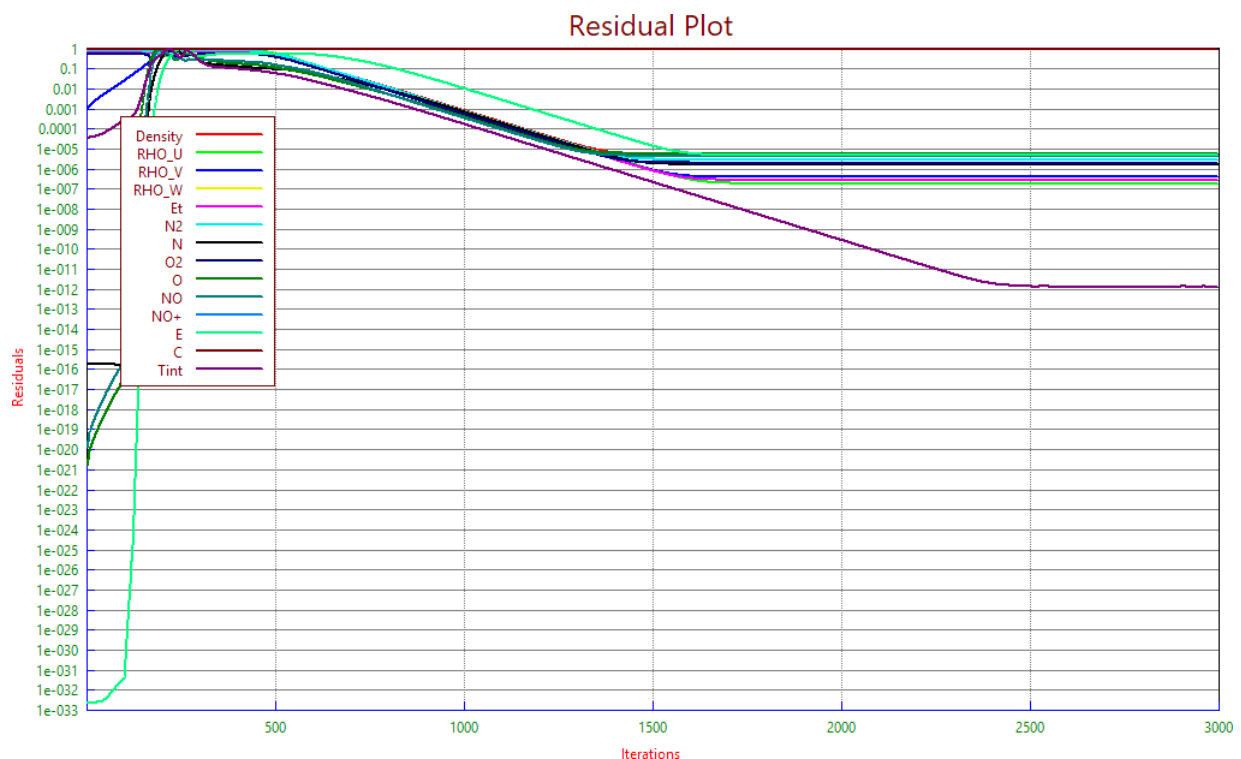


Figure 48. Residual plot – 61 km,  $M = 23.9$ ,  $Re = 1.95 \times 10^4$



Figure 49. Residual plot – 71 km,  $M = 25.9$ ,  $Re = 6.28 \times 10^3$



Figure 50. Residual plot – 81 km,  $M = 28.3$ ,  $Re = 1.59 \times 10^3$

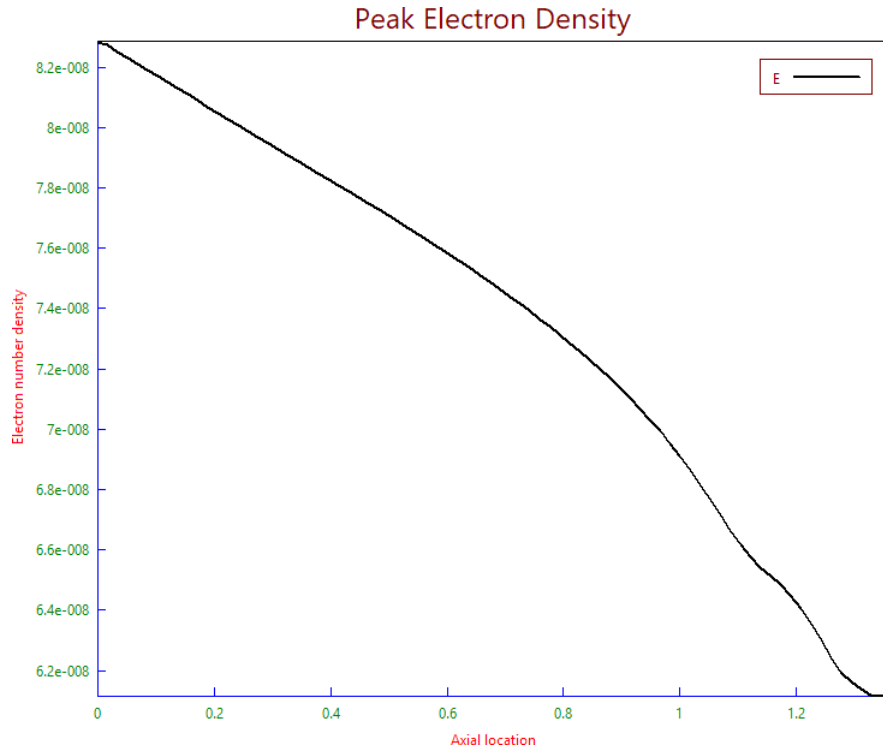


Figure 51. Electron number density – 61 km,  $M = 23.9$ ,  $Re = 1.95 \times 10^4$

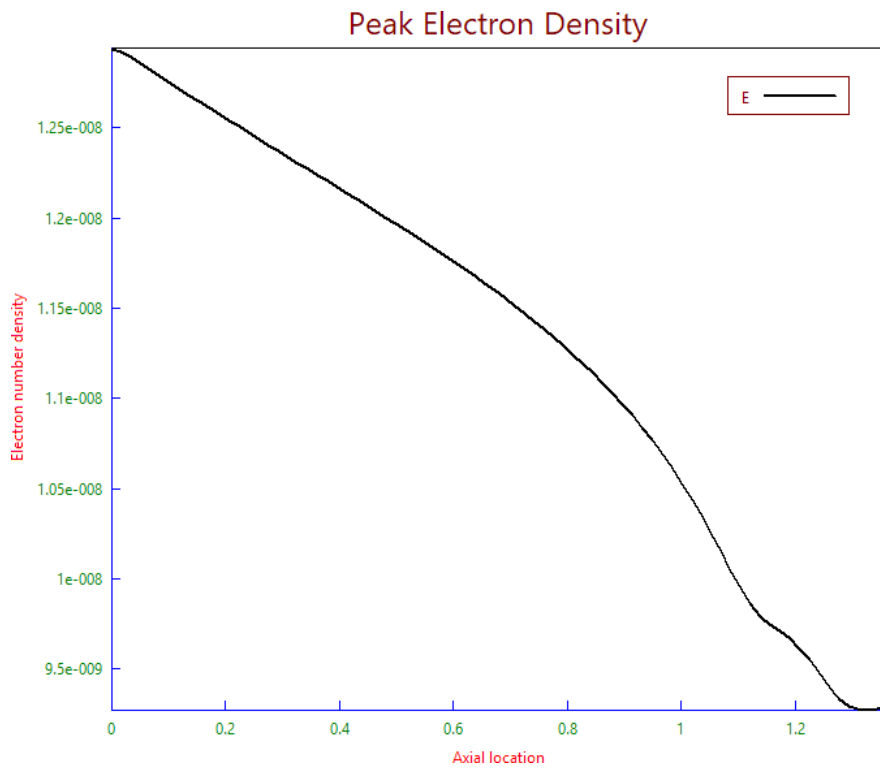


Figure 52. Electron number density – 71 km,  $M = 25.9$ ,  $Re = 6.28 \times 10^3$

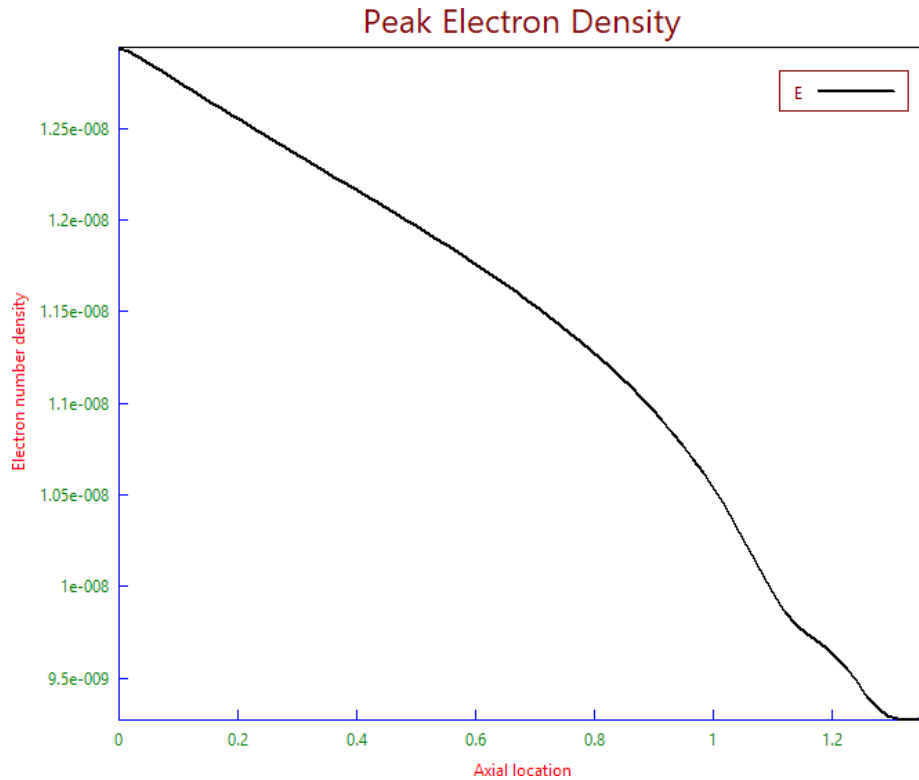


Figure 53. Electron number density – 81 km,  $M = 28.3$ ,  $Re = 1.59 \times 10^3$

From observing the plots in the figures above the electron number density for each of the three cases, there is some difference between the plots compared to the referenced work (MacCormack, Candler 1991). However, plots from both the present and referenced work (MacCormack, Candler 1991), do show similarities regarding the electron number density peaking at the stagnation point, that being at the nose. The electron number density peaks at the nose and greatly reduces along the body and towards the shoulder, which can be seen in the plots including plots from the referenced work (MacCormack, Candler 1991). There's a possibility of some discrepancies either in the settings for the solver or the molecular properties of the species which might be contributing to the way the plots are for the electron number density. Further investigation will be conducted for future work including running more simulations with a different set of parameters regarding the solver. Although, this is a good starting point seeing that there is some agreement regarding the reduction of the electron number density as the gas expands axially along the body. The next set of figures below display contours of mass fractions for nitrogen gas ( $N_2$ ) and oxygen gas ( $O_2$ ) as well as the mass fractions of the major constituents in the reactions.

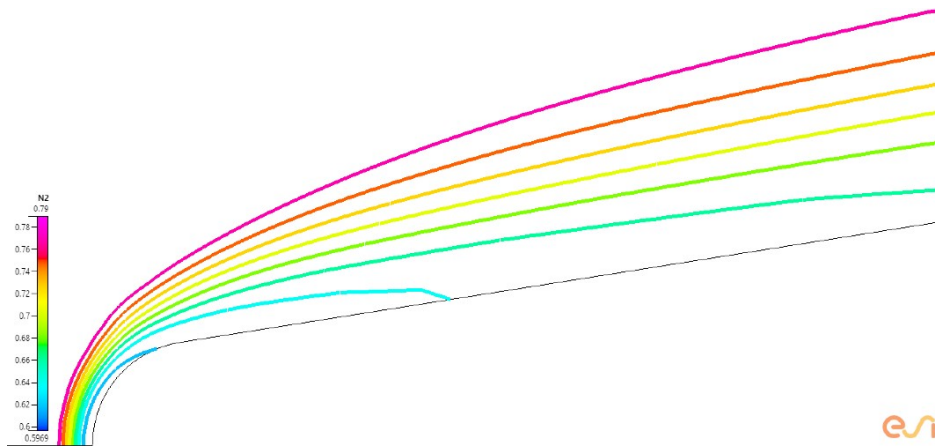


Figure 54. Contours of  $N_2$  mass fraction % – 71 km

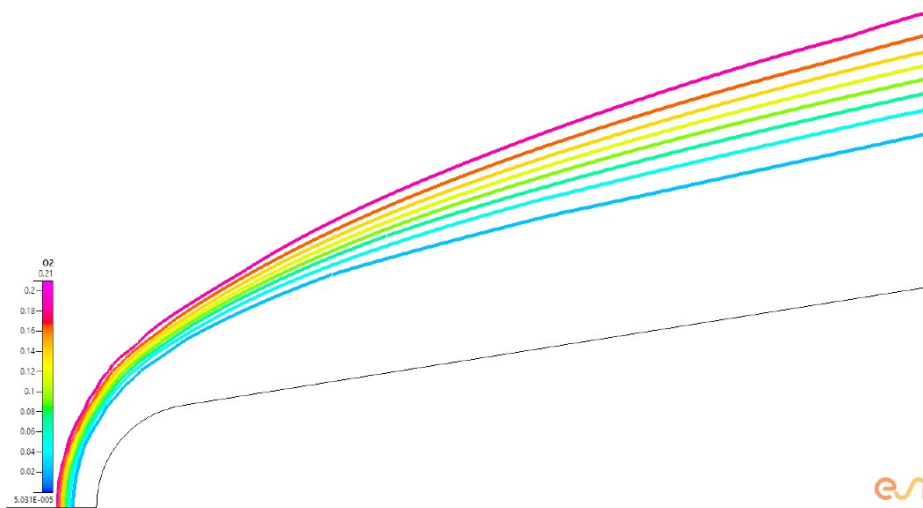


Figure 55. Contours of  $O_2$  mass fraction % – 71 km

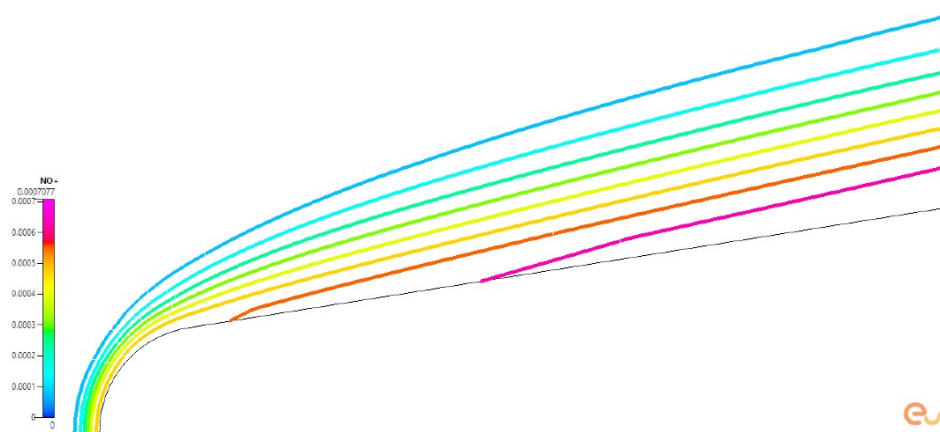


Figure 56. Contours of  $NO^+$  mass fraction % – 71 km

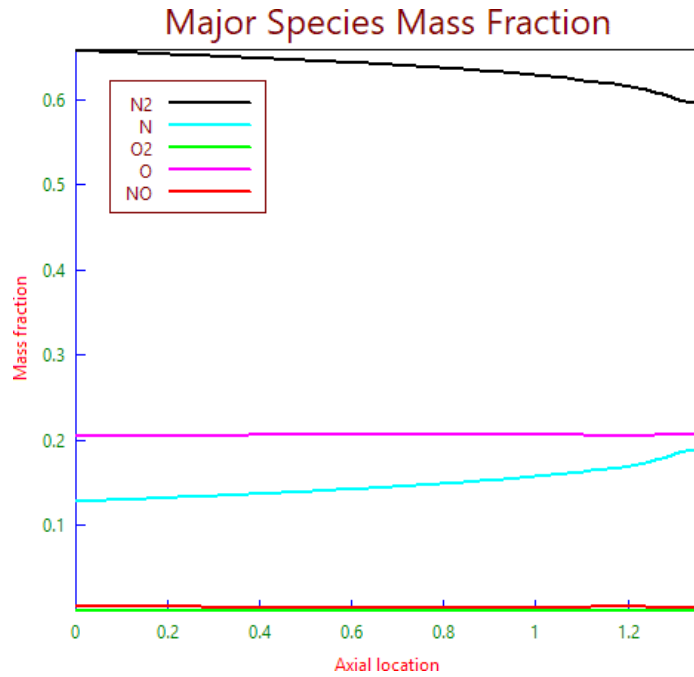


Figure 57. Mass fraction of the five major species – 61 km

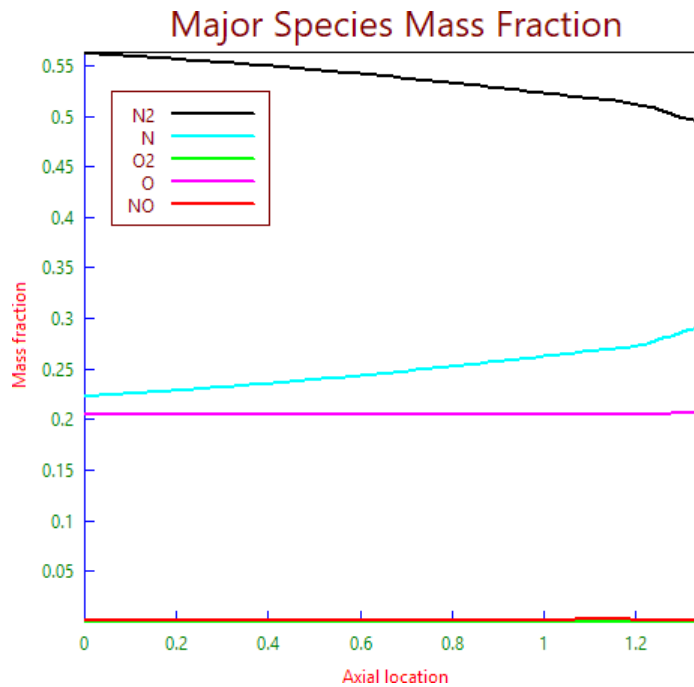


Figure 58. Mass fraction of the five major species – 71 km

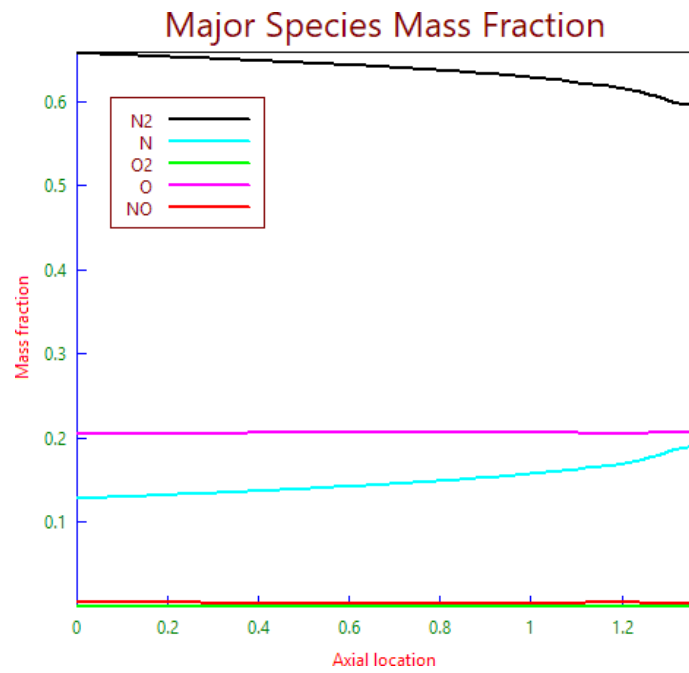


Figure 59. Mass fraction of the five major species – 81 km

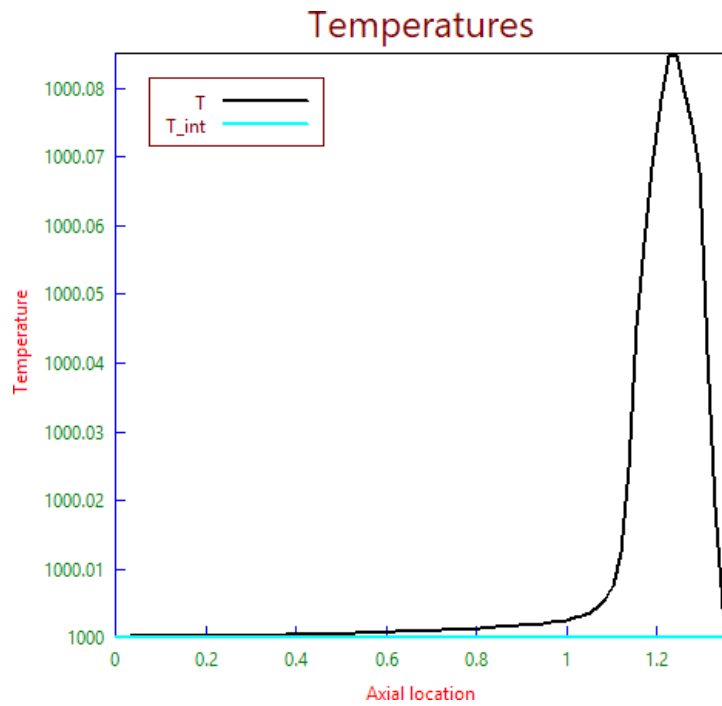


Figure 60. Temperatures on the stagnation streamline – 71 km

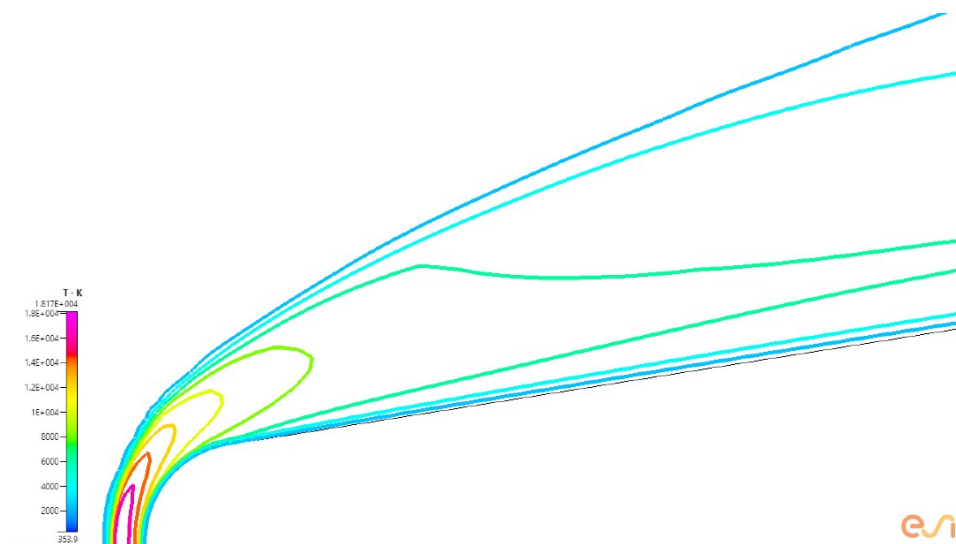


Figure 61. Temperature distribution axial on the body – 71 km

After a complete analysis of the simulations conducted and its results, it can clearly be seen that there are some possible discrepancies between the present and referenced work (MacCormack, Candler 1991). However, those discrepancies, if any, can be mitigated in order to achieve and one to one match in terms of the results. Nevertheless, there are some agreements between the results from both works. This is evident when observing the contours of the mass fractions, for both the nitrogen gas and oxygen gas. There is, however, for  $NO^+$  (nitric oxide), some difference when looking closely at the contours of its mass fraction. This indifference could be explained by looking at the coupled equations that describe the kinetic chemistry or possibly a discrepancy in the molecular properties in which some were made via assumptions.

Another set of indifferences can be seen in the plots for the five major species and its mass fraction percentages. Those discrepancies could possibly be explained, once again, by the parameters defined in the molecular properties which could have contributed to the results of the present work to have some indifference towards the referenced work (MacCormack, Candler 1991). Although, there is agreement in the temperatures when looking at Figure 61. It can be seen in Figure 61, that the temperatures are greatest at the stagnation point which is at the nose and this shows agreement for the electron number density. Because the air dissociates due to high temperatures during re-entry, the nose of the body would have the highest peak of the local temperatures, generating free electrons, with its highest buildup of free electrons at the nose. Whatever indifferences that exist within different parts of the results, it cannot be ignored, that there is agreement in other aspects regarding mass fractions or temperatures at the stagnation point, or even the electron number density axially on the body.

## **6.1 Conclusion**

The validation analysis of the referenced work (MacCormack, Candler 1991) has been completed, however, leaves some work to be done regarding discrepancies seen in the results generated from the simulations. Commercial solvers such as FASTRAN, was found to be more than capable of solving the fully coupled equations that describe two temperature nonequilibrium model for a hypersonic flow field. Although, there are some distinct parameters which were set using the method developed in the referenced work (MacCormack, Candler 1991) that is automatically solved in FASTRAN, and this is regarding the six temperatures, translational-rotational, vibrational, and free electron translational. It's possible that these temperatures could be manually inputted as supposed to being automatically determined in the simulation process, which should be investigated further. There is, however, more than a good amount of promise shown by the results regarding a more important aspect, the electron number density. It was shown to be on a good agreement with the referenced work (MacCormack, Candler 1991) for all three cases. In order to accurately describe the various thermal states of the gas using the conditions set for both the referenced and present work, a multitemperature gas model is required.

The time marching technique used by FASTRAN was able to solve the fully coupled equations including any set of equations which are numerically stiff for all three cases within 3,000 cycles. However, due to the large sets of equations that must be solved due to the complex description of a high velocity flow field, and this makes computations very intensive. Because of this, there were limitations on the computing resources used, which for the present work a personal laptop was used. Using a personal laptop to conduct all simulations limits the use of refined grids of a very high degree, where compromises were made to the grid resolution while maintaining a high quality. However, there are further improvements to be made on the parameters in order to lower the ratio of accuracy at 1 to 1.

## **6.2 Future work**

There is high confidence in the progression of this project with high motivation of continuing it to PhD level research. The discrepancies will be an interesting aspect to look at in terms of increasing the validation percentage of the referenced work (MacCormack, Candler 1991) used. Considering the use of other solvers or developing one are possibilities especially if high fidelity is the objective when using referenced works of all kinds in furthering the validation of various models used. Another consideration is to use more robust methods to solve the fully coupled set of equations that describe these high velocity flows. An interesting piece of software

to look into, is one from Tech-X Corp, known as USim, which is an Euler and N-S solver that has been used before in the simulating plasma blackout cases. There are several existing works supporting the robustness of USim. The use of more powerful computation resources would be most helpful in dealing with the intensity of the large set of equations. Access to better computing resources will also increase confidence by increasing the resolution of the grid to fully capture the interactions in the flow field and the formation of the plasma sheath. This will most definitely to better in achieving higher quality solutions as well as increase the confidence in its accuracy.

## **7.0 Acknowledgements**

First of all, I want to thank my parents for all their support in my academic endeavors, and being an inspiration for the work ethic and the drive that they've instilled in me at a very young age. I want to take this opportunity to thank San Jose State University for providing me with the access to a large knowledge base that has helped me through the completion of the present work. I also want to give thanks to the Aerospace Engineering Department – especially Dr. Nikos Mourtos, for allowing me to pursue this topic to its completion. Lastly, but not the least, I want to give many thanks to my advisor, Dr. Periklis Papadopoulos, who has been an inspirational mentor, not only for helping me understand the importance of the topic I undertook, but also for being as determined as I am to see this present work to completion and having me as his understudy.

## 8.0 References

1. Abhilasha, A. & Boyd, I. (2015). Numerical analysis of surface chemistry in high-enthalpy flows. *Journal of Thermophysics and Heat Transfer*, 29, 653-670. Retrieved March 7, 2017 from AIAA (American Institute of Aeronautics and Astronautics) database.
2. Anderson, J. D. (2006). *Hypersonic and high-temperature gas dynamics* (2nd ed.). Reston, VA: AIAA (American Institute of Aeronautics and Astronautics).
3. Boyd, I. (2007). Modeling of plasma formation in rarefied hypersonic entry flows. *45<sup>th</sup> AIAA Aerospace Sciences Meeting and Exhibit*. Retrieved October 5, 2017 from AIAA (American Institute of Aeronautics and Astronautics) database.
4. Davis, C. N., Peterson, P. Y., & Bilen, S. G. (2011). Hypersonic or re-entry plasma communication. *17<sup>th</sup> AIAA International Space Planes and Hypersonic Systems and Technologies Conference*. Retrieved April 21, 2017 from AIAA (American Institute of Aeronautics and Astronautics) database.
5. Deutschmann, O., Riedel, U., & Warnatz, J. (1994). Modelling of surface reactions in hypersonic re-entry flow fields. *Proceedings of the European Symposium on Aerothermodynamics for Space Vehicles*. Retrieved March 9, 2017 from <http://www.iwr.uni-heidelberg.de/groups/reaflow/user/OLD/riedel/papers/09.pdf>
6. DLR, Stanford work on method for communicating with spacecraft during re-entry (n.d.). Retrieved February 20, 2017 from Parabolic ARC Website <http://www.parabolicarc.com/2016/02/28/dlr-communicatioNavier-Stokestory/>
7. Ito, T., Takaki, R., & Teraoka, K. (1999). Plasma electron density measurement around hypersonic flight experiment vehicle. *Journal of Spacecraft and Rockets*, 36, 573-578. Retrieved July 17, 2017 from AIAA (American Institute of Aeronautics and Astronautics) database.
8. Gillman, E. D., & Foster, J. E. (2009). Investigation of an RF plasma afterglow with a cathode-spot driven quenching method for spacecraft re-entry blackout mitigation. *IEEE International Conference on Plasma Science - Abstracts, ICOPS*. Retrieved March 2, 2017 from IEEE Xplore Digital Library database.
9. Gnoffo, P. A., Gupta, R. N., & Shinn, J. L. (1989). *Conservation equations and physical models for hypersonic air flow in thermal and chemical nonequilibrium* (Report No. NASA-TP-2867). Hampton, VA: NASA Langley Research Center.
10. Group, ESI (2016). *CFD-FASTAN v2017.0 user manual*. Huntsville, AL: Cummings Research Park.

11. Gupta, R. N., Yos, J. M., Thompson, R. A., Lee, K. P. (1990). *A review of reaction rates and thermodynamic and transport properties for an 11-species air model and chemical and thermal nonequilibrium calculations to 30,000 K* (Report No. NASA-RP- 1232). Hampton, VA: NASA Langley Research Center.
12. Kennet, H., & Taylor, R. A. (1966). Earth re-entry simulation of planetary entry environment. *Journal of Spacecraft and Rockets*, 3, 504-512. Retrieved August 7, 2017 from AIAA (American Institute of Aeronautics and Astronautics) database.
13. Kim, M. K. (2009). *Electromagnetic manipulation of plasma layer for re-entry blackout mitigation* (Doctor of Philosophy, The University of Michigan). Retrieved March 1, 2017 from <http://ngpdlab.engin.umich.edu/files/papers/Kim.pdf>
14. Kim, M., Keidar, M., Boyd, I. (2009). Two-dimensional model of an electromagnetic layer for the mitigation of communications blackout. *47<sup>th</sup> AIAA Aerospace Sciences Meeting*, Retrieved September 9, 2017 from AIAA (American Institute of Aeronautics and Astronautics) database.
15. Krishnamoorthy, S., & Close, S. (2017). Investigation of plasma-surface interaction effects on pulsed electrostatic manipulation for reentry blackout alleviation. *Journal of Physics D: Applied Physics*, 50, 1-15. Retrieved September 26, 2017 from IOP Science database.
16. Kundrapu, M., Loverich, J., Beckwith, K., & Shashurin, A. (2014). Electromagnetic wave propagation in the plasma layer of a reentry vehicle. *Proceedings of ICOPS/BEAMS 2014*. Retrieved November 22, 2017 from ResearchGate database.
17. Kundrapu, M., Loverich, J., Beckwith, K., & Shashurin, A. (2013). Modeling and simulation of weakly ionized plasmas using nautilus. *51<sup>st</sup> AIAA Aerospace Sciences Meetings*. Retrieved November 22, 2017 from ResearchGate database.
18. Lehnert, R., & Rosenbaum, B. (1965). *Plasma effects on Apollo re-entry communication* (Report No. NASA-TN-D-2732). Greenbelt, MD: NASA Goddard Space Flight Center.
19. Lomax, H., Pulliam, T. H., & Zingg, D. W. (2011). *Fundamentals of computational fluid dynamics*. Berlin, Germany: Springer-Verlag Berlin Heidelberg.
20. MacCormack, R. W., & Candler, G. V. (1991). Computation of weakly ionized hypersonic flows in thermochemical nonequilibrium. *Journal of Thermophysics and Heat Transfer*, 3, 266-273. Retrieved July 2, 2017 from AIAA (American Institute of Aeronautics and Astronautics) database.
21. Mather, D. E., Pasqual, M. J., Sillence, J. P. (2005). Radio frequency (RF) blackout during hypersonic reentry. *13<sup>th</sup> AIAA/CIRA International Space Planes and Hypersonic Systems*

- and Technologies*. Retrieved June 21, 2017 from AIAA (American Institute of Aeronautics and Astronautics) database.
22. Muylaert, J., Walpot, L., Ottens, H., & Cipollini, F. (2007). Aerothermodynamics re-entry flight experiments expert. *Flight Experiments for Hypersonic Vehicle Development*, 13, 13-1 – 13-34. Retrieved February 2, 2017 from <https://www.sto.nato.int/publications/STO%20Educational%20Notes/RTO-EN-AVT-130/EN-AVT-130-13.pdf>
  23. Park, C. (1989). Assessment of two-temperature kinetic model for ionizing air. *Journal of Thermophysics and Heat Transfer*, 3, 233-244. Retrieved July 2, 2017 from AIAA (American Institute of Aeronautics and Astronautics) database.
  24. Park, C. (1988). Assessment of two-temperature kinetic model for dissociating and weakly ionizing nitrogen. *Journal of Thermophysics and Heat Transfer*, 1, 8-16. Retrieved July 2, 2017 from AIAA (American Institute of Aeronautics and Astronautics) database.
  25. Park, C. (1993). Review of chemical-kinetic problems of future NASA missions, i: earth entries. *Journal of Thermophysics and Heat Transfer*, 7, 385-398. Retrieved July 21, 2017 from AIAA (American Institute of Aeronautics and Astronautics) database.
  26. Park, C. (1985). *On convergence of computation of chemically reacting flows*. (Report No. 85-0247). Moffett Field, CA: NASA Ames Research Center.
  27. Park, C., Jaffe, R., & Partridge, H. (2001). Chemical-kinetic parameters of hyperbolic earth entry. *Journal of Thermophysics and Heat Transfer*, 15, 76-89. Retrieved March 4, 2017 from AIAA (American Institute of Aeronautics and Astronautics) database.
  28. Rybak, J. P. (1970). *Causes, effects and diagnostic measurements of the re-entry plasma sheath* (Report No. 1). Fort Collins, CO: Colorado State University.
  29. *Satellite communications and space weather*. (n.d.). Retrieved February 3, 2017 from Australian Government Bureau of Meteorology Space Weather Services Website <http://www.sws.bom.gov.au/Educational/1/3/2>
  30. Shao, C., Deyang, T., Chen, W. (2016). Numerical simulation of time-varying plasma sheath for reentry vehicle. *34<sup>th</sup> AIAA Applied Aerodynamics Conference*. Retrieved February 21, 2017 from AIAA (American Institute of Aeronautics and Astronautics) database.
  31. Scintillation effect on satellite communications within standard atmosphere. (2009). *Anbar Journal of Engineering Sciences*, 2, 17-27. Retrieved February 20, 2017 from <https://www.iasj.net/iasj?func=fulltext&ald=14227>

32. Takahashi, Y., Nakasato, R., & Oshima, N. (2016). Analysis of radio frequency blackout for a blunt-body capsule in atmospheric re-entry missions. *Aerospace – Open Access Aeronautics and Astronautics Journal*, 3, 1-19. Retrieved March 5, 2017 from MDPI (Multidisciplinary Digital Publishing Institute) database.
33. Takahashi, Y., Yamada, K., & Abe, T. (2014). Prediction performance of blackout and plasma attenuation in atmospheric reentry demonstrator mission. *Journal of Spacecraft and Rockets*, 51, 1954-1964. Retrieved July 19, 2017 from AIAA (American Institute of Aeronautics and Astronautics) database.
34. Takahashi, Y. (2015). Advanced validation of cfd-fdtd combined method using highly applicable solver for reentry blackout problem. *Journal of Physics D: Applied Physics*, 49, 1-15. Retrieved September 18, 2017 from IOP Science database.
35. *The ionospheric effect*. (n.d.) Retrieved March 2, 2017 from PennState College of Earth and Mineral Sciences Website <https://www.e-education.psu.edu/geog862/node/1715>
36. Weaver, W. L. (1972). *Multiple-orifice liquid injection into hypersonic air streams and application to RAM C-III flight* (Report No. NASA-TM-X-2486). Hampton, VA: NASA Langley Research Center.
37. Weaver, W. L., & Bowen, J. T. (1972). *Entry trajectory, entry environment, and analysis of spacecraft motion for the RAM C-III experiment* (Report No. NASA-TM-X-2562). Hampton, VA: NASA Langley Research Center.
38. Webb, H., Dresser H., Korkan, K., Raparelli, R. (1969). *Theoretical flow field calculations for project ram* (Report No. NASA-CR-1308). Downey, CA: North American Rockwell Corporation.
39. Whitney, H. E., & Basu, S. (1977). The effect of Ionospheric scintillation on VHF/UHF satellite Communications. *Radio Science*, 12, 123-133. Retrieved February 16, 2017 from IEEE Xplore Digital Library database.
40. Wright, M. J., Loomis, M., Papadopoulos, P. (2003). Aerothermal analysis of the project fire II afterbody flow. *Journal of Thermophysics and Heat Transfer*, 17, 240-249. Retrieved February 10, 2017 from AIAA (American Institute of Aeronautics and Astronautics) database.
41. Wright, M. J., Prabhu, D. K., Martinez, E. R. (2006). Analysis of Apollo command module afterbody heating part I: AS-202. *Journal of Thermophysics and Heat Transfer*, 20, 16-30. Retrieved March 17, 2017 from AIAA (American Institute of Aeronautics and Astronautics) database.

42. Wright, M. J., Milos, F. S., Tran, P. (2006). Afterbody aeroheating flight data for planetary probe thermos protection system design. *Journal of Spacecraft and Rockets*, 43, 929-943. Retrieved February 19, 2017 from AIAA (American Institute of Aeronautics and Astronautics) database.
43. Yakovlev, O., Matyugov, S., & Vilkov, I. (1995). Attenuation and scintillation of radio waves in the Earth's atmosphere from radio occultation experiments on satellite-to-satellite links. *Radio Science*, 30, 591-602. Retrieved February 12, 2017 from IEEE Xplore Digital Library database.
44. Zubair, M., Haider, Z., Khan, S. A., & Nasir, J. (2011). Atmospheric influences on satellite communications. *Przegląd Elektrotechniczny – Electrical Review*, 87, 261-264. Retrieved February 22, 2017 from ResearchGate database.

## 9.0 Appendices

### I. **Appendix A.** Script for CFD-FASTRAN (Python) – unused in the simulations.

#### Apollo Command Module - sample

```
import GuiVersion
import GuiDBM
import GuiFILE
import GuiML
import GuiPT
import GuiMO
import GuiVC
import GuiBC
import GuiIC
import GuiPC
import GuiFan
import GuiMacP
import GuiMR
import GuiMRF
import GuiSC
import GuiOut
import GuiRun

#The following line is for backwards-compatibility, DO NOT DELETE IT.
GuiVersion.RecordVersion("2016.0.0.11217")

GuiFILE.SetMode("FASTRAN")
GuiFILE.Open("C:/Users/spl4ckd/Documents/Aerospace.Courses/AE.295.A_B/Plasma
Blackout/CFD/Apollo_CM/drive-download-20170824T211728Z-001/18_14 -
Copy/Apollo_CM_18_14.DTF")
```

#### RAM C-II - sample

```
import GuiVersion
import GuiDBM
import GuiFILE
import GuiML
import GuiPT
import GuiMO
import GuiVC
import GuiBC
import GuiIC
import GuiPC
import GuiFan
import GuiMacP
import GuiMR
import GuiMRF
import GuiSC
import GuiOut
import GuiRun

#The following line is for backwards-compatibility, DO NOT DELETE IT.
GuiVersion.RecordVersion("2017.0.0.11893")

GuiFILE.SetMode("FASTRAN")
```

## II. Appendix B. Euler equations

$$\frac{\partial Q}{\partial t} + \frac{\partial E}{\partial x} + \frac{\partial F}{\partial y} = 0$$

$$Q = \begin{bmatrix} q_1 \\ q_2 \\ q_3 \\ q_4 \end{bmatrix} = \begin{bmatrix} \rho \\ \rho u \\ \rho v \\ e \end{bmatrix}, E = \begin{bmatrix} \rho u \\ \rho u^2 + p \\ \rho uv \\ u(e + p) \end{bmatrix}, F = \begin{bmatrix} \rho v \\ \rho uv \\ \rho v^2 + p \\ v(e + p) \end{bmatrix}$$

$$p = (\gamma - 1) \left( E - \frac{1}{2} \rho (u + v) \right)$$

## III. Appendix C. Navier-Stokes equations

- Continuity:

$$\frac{\partial \rho}{\partial t} + \frac{\partial(\rho u)}{\partial x} + \frac{\partial(\rho v)}{\partial y} + \frac{\partial(\rho w)}{\partial z} = 0$$

- X-Momentum:

$$\frac{\partial(\rho u)}{\partial t} + \frac{\partial(\rho u^2)}{\partial x} + \frac{\partial(\rho uv)}{\partial y} + \frac{\partial(\rho uw)}{\partial z} = - \frac{\partial P}{\partial x} + \frac{1}{Re_r} \left( \frac{\partial \tau_{xx}}{\partial x} + \frac{\partial \tau_{xy}}{\partial y} + \frac{\partial \tau_{xz}}{\partial z} \right)$$

- Y-Momentum:

$$\frac{\partial(\rho v)}{\partial t} + \frac{\partial(\rho v^2)}{\partial y} + \frac{\partial(\rho uv)}{\partial x} + \frac{\partial(\rho vw)}{\partial z} = - \frac{\partial P}{\partial y} + \frac{1}{Re_r} \left( \frac{\partial \tau_{xy}}{\partial x} + \frac{\partial \tau_{yy}}{\partial y} + \frac{\partial \tau_{yz}}{\partial z} \right)$$

- Z-Momentum:

$$\frac{\partial(\rho w)}{\partial t} + \frac{\partial(\rho w^2)}{\partial z} + \frac{\partial(\rho uw)}{\partial x} + \frac{\partial(\rho vw)}{\partial y} = - \frac{\partial P}{\partial z} + \frac{1}{Re_r} \left( \frac{\partial \tau_{xz}}{\partial x} + \frac{\partial \tau_{yz}}{\partial y} + \frac{\partial \tau_{zz}}{\partial z} \right)$$

- Energy:

$$\begin{aligned} \frac{\partial(E_T)}{\partial t} + \frac{\partial(uE_T)}{\partial x} + \frac{\partial(vE_T)}{\partial y} + \frac{\partial(wE_T)}{\partial z} &= - \frac{\partial(uP)}{\partial x} - \frac{\partial(vP)}{\partial y} - \frac{\partial(wP)}{\partial z} \\ &= \frac{1}{Re_r Pr_r} \left( \frac{\partial q_x}{\partial x} + \frac{\partial q_y}{\partial y} + \frac{\partial q_z}{\partial z} \right) + \frac{1}{Re_r} \\ &\quad \left( \frac{\partial}{\partial x} (u\tau_{xx} + v\tau_{xy} + w\tau_{xz}) + \frac{\partial}{\partial y} (u\tau_{xy} + v\tau_{yy} + w\tau_{yz}) + \frac{\partial}{\partial z} (u\tau_{xz} + v\tau_{yz} + w\tau_{zz}) \right) \end{aligned}$$

#### IV. Appendix D. Computed flow field equations

- Mass conservation of the species:

$$\frac{\partial \rho_s}{\partial t} + \frac{\partial(\rho u)}{\partial x_j} = - \frac{\partial(\rho_s v_{sj})}{\partial x_j} + W_s$$

- Mass-averaged momentum:

$$\frac{\partial(\rho u_s)}{\partial t} + \frac{\partial(\rho u_i u_j)}{\partial x_j} = - \frac{\partial(\tau_{ij})}{\partial x_j} + \sum_s e_s N Z_{s s i} E$$

- Vibrational energy:

$$\frac{\partial E_{vs}}{\partial t} + \frac{\partial(E_{vs} u_j)}{\partial x_j} = - \frac{\partial(E_{vs} v_{sj})}{\partial x_j} - \frac{\partial q_{vsj}}{\partial x_j} + Q_{\tau-us} + Q_{v-us} + Q_{e-us} + w_{s us} e$$

- Electron energy:

$$\begin{aligned} \frac{\partial E_e}{\partial t} + \frac{\partial [(E_e + \rho_e) u_j]}{\partial x_j} &= - \frac{\partial [(E_e + \rho_e) v_{ej}]}{\partial x_j} - \frac{\partial q_{ej}}{\partial x_j} - \frac{\partial [(u_i + v_{ei}) \tau_{eij}]}{\partial x_j} + N_e e \tilde{E} (u_i + v_{ei}) + Q_{\tau-e} - \\ &\quad \sum_s Q_{e-vs} + w_{e e} \end{aligned}$$

- Total energy:

$$\frac{\partial E}{\partial t} + \frac{\partial [(E + \rho) u_j]}{\partial x_j} = - \frac{\partial (q_j + q_{vj} + q_{ej})}{\partial x_j} - \frac{\partial (u_i \tau_{ij})}{\partial x_j} - \frac{\partial}{\partial x_j} \sum_s v_{s s j} \rho h_{s s} + \sum_s e N Z_{s s i} E u_{s i}$$

V. **Appendix E.** Seven species reaction model

- $N_2 + M \rightleftharpoons 2N + M$
- $O_2 + M \rightleftharpoons 2O + M$
- $NO + M \rightleftharpoons N + O + M$
- $N_2 + O \rightleftharpoons NO + N$
- $NO + O \rightleftharpoons O_2 + N$
- $N + O \rightleftharpoons NO^+ + e^-$